MONTE CARLO SIMULATION OF PN-JUNCTIONS

by

Camilla Nestande Kirkemo

THESIS

for the degree of

MASTER OF SCIENCE

(Master in Computational Physics)

Faculty of Mathematics and Natural Sciences
University of Oslo

September 2011

Det matematisk- naturvitenskapelige fakultet
Universitetet i Oslo

Contents

1 Introduction **5**

2 Basics of modelling semiconductors **9**

2.1 Semiconductor materials 9
2.2 $Cd_xHg_{1-x}Te$ 10
2.3 Quantum mechanical treatment of crystals 11
2.4 Boltzmann's transport equation 13
2.5 Scattering events 15
2.6 Applying the theory to the particle simulator 16

3 The Monte Carlo simulator **19**

3.1 Description of the program 20
3.2 Device geometry 23
3.3 Carrier dynamics 23
3.4 Particle-mesh coupling 25
3.5 Ohmic contacts 27
3.6 Measuring current 29
3.7 Boundary conditions 30
3.8 Modelling 3D devices in 2D 31
3.9 Superparticles in 2D and 3D 31

4 Poisson's equation **33**

4.1 Poisson's equation in a material 33
4.2 The finite difference formulation 34
4.3 Boundary conditions 35
4.4 Overview of numerical methods 36
4.5 The relaxation methods 37
4.6 Parallellising the Poisson solver 40

5 Accuracy and reliability of the model **41**
5.1 Resolution in time and space . . . 41
5.2 Mobility . . . 43
5.3 Simulation of an n+ n n+ diode . . . 44

6 PN junction **47**
6.1 Simulation parameters and assumptions . . . 47
6.2 Simulation results under reverse bias . . . 49
6.3 Simulation results under forward bias voltage . . . 56
6.4 IV characteristics of the *pn* junction . . . 58
6.5 Switching behaviour of a diode . . . 60

7 APD model **65**
7.1 Principle of operation . . . 65
7.2 APD architecture . . . 66
7.3 The Auger and impact ionisation processes . . . 67
7.4 The impact ionisation model . . . 68
7.5 Overview of program implementation . . . 73

8 APD simulation results **77**
8.1 Distribution of carriers inside the device . . . 77
8.2 Switching time . . . 78
8.3 Multiplication and noise . . . 78
8.4 Current impulse response . . . 81
8.5 Gain-voltage characteristics . . . 82

9 Discussion and further work **85**
9.1 Further work . . . 86

10 Conclusions **89**

Appendices **89**

A Energybands and effective masses **91**

B Scattering rates **93**

Bibliography **102**

Chapter 1

Introduction

The information age, in which we live, is based on digital computers and electronic devices made possible by the use of semiconductor devices. Yet, understanding these devices is a challenge; in the research field of semiconductors it is not unusual that a device is produced in a laboratory before the physics of the material is fully understood. In order to obtain the detailed knowledge of how these devices really work, it is necessary to model the physical processes taking place at a microscopic scale inside the material. Modern microelectronic devices requires the treatment of transient dynamics of highly non-equilibrium carrier distributions; the Monte Carlo method of semiconductor device simulation is a widely used and acknowledged model suitable for this purpose. The method is a computer simulation technique where the model is designed on a microscopic scale, on the level of electronic interactions, while the results are obtained in terms of macroscopic material properties, e.g. the current-voltage characteristics of a diode. Using computer simulation techniques such as the Monte Carlo method offers a unique insight into processes which are not directly observable in physical experiments.

The Monte Carlo method is a particle simulation technique where we follow the phase space trajectories of the current conducting particles in a semiconductor material. These particles are subject to thermal motion within a crystal lattice. This is modelled as a series of free flights terminated by scattering events. Random numbers are used to determine the duration of the free flights and the new directions of the particles after the scatterings. In this way, we obtain the statistical distribution of particle states in the

material which is also a solution to Boltzmann's transport equation. All macroscopic transport properties may be extracted from this solution as ensemble or time averages.

For our purposes, which is device simulation, the electric field within the device also needs to be considered, and hence it is the solution to the self-consistent system of system of Boltzmann's equation and Poisson's equation that needs to be obtained. In this thesis, an iterative fast Poisson solver suitable for two-terminal devices has been developed and an Ohmic contact model has been implemented to the existing bulk simulator.

The Monte Carlo method for material simulations roots in the 1960's, and has been the base for numerous publications during the past fifty years. It has been recognised as a powerful theory for studying physics on the border between the classical and quantum mechanical regimes. A way to view this is considering the effort that has been put into stretching the temporal and spatial validity regime of the model. In the limit of long simulation times, the method is used in combination with hydrodynamic theory which allows a longer time step. In the limit of small devices, a variety of quantum correction methods have been developed.

In this thesis, we have used the Monte Carlo method for semiconductor device simulation to simulate a *pn*-diode and an avalanche photodiode (APD). A *pn*-diode is a rectifying device which allows current to pass in one direction while current in the opposite direction is blocked. The APD is a highly sensitive photo-detector which relies on the photoelectric effect; a photon excites an electron into the conduction band, the APD then exploits the physical process of impact ionisation to generate an avalanche of carriers. This gives rise to a current pulse which is large enough to be detectable in the electrical circuit surrounding the diode. APDs are increasingly important for technological applications; they are used as detecting components of LIDARs, which are used for optical remote sensing, and for scintillation detectors, which measure ionising radiation.

The APD and the *pn*-diode are both relatively simple two-terminal devices in which the *pn*-junction constitute the main building block. Simple components like these have traditionally been analysed using the drift-diffusion or hydrodynamic model. Particle simulation techniques have not, to any great extent, been employed to this task. In this thesis, we apply the Monte Carlo method to *pn*-junction devices in order to investigate some of the limits and weaknesses of the Monte Carlo method.

Stationary simulations of a *pn*-diode have been conducted in order to obtain the current-voltage characteristics for the device. It points to the fact that the Monte Carlo method is unsuited for obtaining the reverse leakage current for $\mathrm{Cd}_x\mathrm{Hg}_{1-x}\mathrm{Te}$ (CMT) *pn*-diodes. Detailed statistics have been extracted for simulations under reverse and forward bias voltage, these indicate that there is a small accumulation of an electron plasma at the *p*-side of the junction of the CMT diode. This phenomenon has previously been observed for GaAs-diodes. A transient simulation has been performed in order to obtain the switching time for the CMT *pn*-diode at a reverse bias of −5 V. In addition, our simulation results show that large electric fields arise across a CMT *pn*-junction, thus it may be necessary to incorporate intracollisional field effects by extending the simulator with quantum corrections.

I order to do simulations of CMT APDs, a simple impact ionisation model has been implemented to the Monte Carlo simulator. Multiplication and noise has been measured under variations in lattice temperature and photon wavelength, the multiplication gain was observed to be slightly higher due to increased mobility in the cooled device. Furthermore, our results show an exponential gain-voltage curve and excess noise which is independent of gain. We report a switching time of 500 ps when the device is switched from the conducting state to a reverse bias voltage of −8 V. We also present the current impulse response time, which points to a weakness of the Monte Carlo model; due to the large asymmetry in the effective masses of electrons and holes in CMT, it is necessary to take into account charge continuity in the surrounding circuit and the displacement current in order to obtain a proper current-response curve.

This thesis is part of a student project which has been undergoing at the Norwegian Defence Research Establishment (FFI) since 2007. The aim of the project is to develop a state of the art Monte Carlo simulation tool for both bulk and devices and thereby promote the photovoltaic infrared detector development taking place at FFI. In this context, the aim of this thesis has been to extend the existing bulk simulator to a device simulator with the implementation of a fast Poisson solver and an ohmic contact model, as well as enabling the study APDs with the implementation of an impact ionisation model.

Chapter 2

Basics of modelling semiconductors

This chapter gives a short introduction to the some of the topics of solid state physics which are needed for modelling semiconductor crystals. The aim is to build a bridge between the theory as it is often presented in quantum mechanics and solid state courses taught at the university and how the theory is used in a Monte Carlo particle simulator. First, the properties of semiconductors in general are briefly summed up in section 2.1 and a few properties of $Cd_xHg_{1-x}Te$ are given in section 2.2. In section 2.3, a brief presentation of the quantum mechanical description of crystals is given, including the concepts of Bloch states and energy bands. In section 2.4, the Boltzmann transport equation is presented, and finally, in section 2.5, the quantum mechanical treatment of scattering events is presented.

2.1 Semiconductor materials

Solid state materials are categorised as metals, semiconductors or insulators based on the electrical conductivity of the material. Semiconductors have lower conductivity than metals, but higher conductivity than insulators. At low temperatures, the valence band is completely filled while the conduction band is empty, thus the semiconductor behaves like an insulator. At room temperature, electrons are thermally excited to the conduction band, and hence the material becomes conductive.

The conductivity of semiconductors is easily controlled, either dynamically by temperature changes or permanently by the level of impurities introduced into the material. This property makes semiconductor materials applicable for a wide range of purposes within the electronics industry.

Semiconductor materials have crystal structure where the atoms are arranged in a periodic lattice. The material may be doped with impurity atoms to modify the electronic properties of the material. In this process, some of the host atoms are replaced by impurity atoms. If arsenic atoms, which have five valence electrons, are implanted into a silicon lattice, four of the valence electrons of each arsenic atom will form covalent bonds with the neighbouring silicon atoms. The fifth electron ends up being loosely bound to its host atom and is therefore easily excited to the conduction band, leaving behind an ionised impurity centre. While donors contribute electrons to the conduction band forming n-type semiconductors, acceptors contribute holes to the valence band that participate in electrical conduction in p-type semiconductors. In this thesis both n- and p-type materials will be considered. The material is assumed to be fully ionised at room temperature, thus the density of conduction band electrons is set equal to the density of donors and likewise the hole density is assumed equal to the acceptor density.

2.2 $Cd_xHg_{1-x}Te$

$Cd_xHg_{1-x}Te$, abbreviated CMT, is a compound ternary alloy semiconductor which crystallises in the zinc blende lattice structure. It is composed of the semimetal HgTe and the semiconductor CdTe; the x denotes the mole fraction of HgTe in the alloy. CMT has a direct bandgap which increases approximately linearly with x until reaching the bandgap of CdTe which is 1.5 eV at room temperature. The band gap is also temperature dependent, an experimentally obtained formula for the bandgap which is valid up to $T = 500$ K is given in [1]:

$$E_g = E_{g0} + \frac{6.3 \cdot (1-x) - 3.25 \cdot x - 5.92 \cdot x \cdot (1-x)}{11 \cdot (1-x) + 78.7 \cdot x + T} \times 10^{-4} T^2,$$

where $E_{g0} = -0.303 \cdot (1-x) + 1.606 \cdot x - 0.132 \cdot x \cdot (1-x)$. E_g is in eV and T in K.

The variable bandgap and the high absorption coefficient makes CMT a very useful material for applications. It can be tuned to absorb wavelengths in

the interval $0.7 - 25$ μm, thus covering most of the infrared region of the electromagnetic spectrum. CMT is an important material to the industry of infrared detectors and photodiodes, and especially useful for fabricating highly sensitive avalanche photodiodes which are low in noise.

The simulations which has been performed during the work with this thesis are done with an alloy fraction of $x = 0.28$ and, unless otherwise stated, at room temperature. These conditions correspond to a bandgap $Eg = 0.27$ eV.

2.3 Quantum mechanical treatment of crystals

The quantum mechanical description of a perfect crystal is thoroughly given in many textbooks, among them [2]. The full description of a perfect crystal is given by the Schrodinger equation with the many particle crystal Hamiltonian

$$\begin{aligned}\mathcal{H} = &\sum_i \frac{p_i^2}{2m_i} + \sum_j \frac{P_j^2}{2M_j} + \frac{1}{2}\sum_{j',j}{}' \frac{Z_j Z_{j'} e^2}{4\pi\varepsilon_0 |\mathbf{R}_j - \mathbf{R}_{j'}|} \\ &- \frac{1}{2}\sum_{j,i}{}' \frac{Z_j e^2}{4\pi\varepsilon_0 |\mathbf{r}_i - \mathbf{R}_j|} + \frac{1}{2}\sum_{i',i}{}' \frac{e^2}{4\pi\varepsilon_0 |\mathbf{r}_i - \mathbf{r}_{i'}|}.\end{aligned}$$

Here, the two first term represents respectively the kinetic energy of the electrons, having masses m_i, and the nuclei of masses M_j. The three last terms represent the potential energies between the ions and the electrons. The symbols $\mathbf{p}_i$ and $\mathbf{P}_j$ represent the momentum operators of the i'th electron and the j'th nucleus, $\mathbf{r}_i$ and $\mathbf{R}_j$ denote their respective positions. Z_j denotes the atomic number of the j'th nucleus and ε_0 the electrical permittivity of vacuum.

To be able to solve this system, we introduce several approximations. First, the nuclei and the strongly bound core electrons are lumped together reducing the system to ion cores and loosely bound conduction electrons. This does not change the appearance of the equation above, but changes the meaning of the indices; i now labels only valence electrons instead of all electrons, and j now labels ion cores.

Next, the Born-Oppenheimer approximation can be applied since the ion cores are heavier and slower than the valence electrons. As a consequence,

the electrons sees only the potential of the stationary ion cores, while the ion cores sees only the time-averaged adiabatic potential of the valence electrons. The Hamiltonian is thereby reduced to a sum of three terms,

$$\mathcal{H} = \mathcal{H}_{ions}(\mathbf{R}_j) + \mathcal{H}_e(\mathbf{r}_i, \mathbf{R}_{j0}) + \mathcal{H}_{e-ion}(\mathbf{r}_i, \delta\mathbf{R}_j).$$

The first term describes the ionic motion in the averaged potential; the second term is denoted the electronic term, it describes the motion of the electrons in the lattice where the ions are frozen in their equilibrium positions, $\mathbf{R}_{j0}$, and the last term describes the change in electronic energies due to displacements, $\delta\mathbf{R}_j$, of the ions from their equilibrium positions, also called phonons.

Further, the mean field approximation, which is derived in [3], is applied. The purpose of this approximation is to reduce the many-body problem above to an effective one-body problem where all electrons are considered to experience the same averaged potential $V(\mathbf{r})$. The result is the familiar one-electron Schrödinger equation:

$$\left(\frac{p^2}{2m} + V(\mathbf{r})\right)\psi_n(\mathbf{r}) = E_n\psi_n(\mathbf{r}). \tag{2.1}$$

Here, ψ_n denotes the one-electron wave function and E_n the one-electron energy of the eigenstate labelled n. Even though they are accurate solutions to 2.1, they are approximate in the sense that the equation is subject to the above mentioned approximations.

The Bloch theorem states that when $V(\mathbf{r})$ is a periodic function, the solutions to 2.1 are Bloch waves,

$$\psi_{n\mathbf{k}}(\mathbf{r}) = e^{i\mathbf{k}\cdot\mathbf{r}}u_{n\mathbf{k}}(\mathbf{r}),$$

where $u_{n\mathbf{k}}(\mathbf{r})$ have the periodicity of the lattice, with corresponding energies

$$E_n = E_n(\mathbf{k}).$$

The solutions carries the index $\mathbf{k}$ which is the wave vector. The allowed electronic states are thus defined by the two indices $\mathbf{k}$ and n. The $\mathbf{k}$-vector takes values within the first Brillouin zone of the reciprocal lattice. The index $n \in [1, \infty)$ represents the available bands. The bands with the lowest indices are valence bands occupied by valence electrons, while the electrons in the conduction band participate in conducting current. The band structure

$E_n(\mathbf{k})$, originating from the periodic nature of the crystal defines the allowed electronic energy states of the crystal.

There are several methods of calculating the band structure of a crystal. Symmetry often aids the calculations, and hence band structure calculations produce $E(\mathbf{k})$-relations along crystal directions of high symmetry, see fig 2.1, within the Brillouin zone. The basis for the band model used with our simulations is the $\mathbf{k} \cdot \mathbf{p}$-method, which is a perturbative method; thus the accuracy of the energy decreases as k increases.

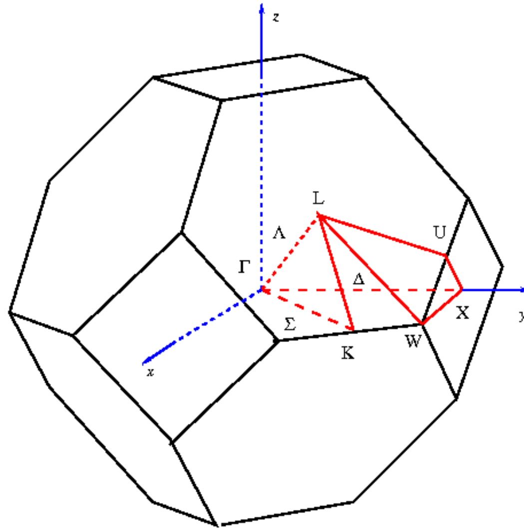

Figure 2.1: First Brillouin zone of the *fcc* crystal lattice with symmetry labels. Figure from [4].

2.4 Boltzmann's transport equation

The transport properties of a material is described by the Boltzmann transport equation. Applied to our system, which is a slab of semiconductor material, the solution to the Boltzmann equation is the statistical distribution function of the conduction band electrons in the material. When the probability of each available phase space state being occupied is known, all transport properties may be evaluated taking averages over a statistical ensemble of carriers.

The Boltzmann transport equation is an equation for the rate of change of

the distribution function. The distribution function, $f = f(\mathbf{r}, \mathbf{k}, t)$, of the electrons is in general a function of position, $\mathbf{r}$; momentum, $\mathbf{k}$ and time, t. It describes the probability of a phase space state being occupied at a given time. In equilibrium, the distribution function is the familiar Fermi-Dirac function,

$$f(E) = \frac{1}{e^{(E-E_F)/k_BT} + 1},$$

which is here stated in terms of energy, E. E_F denotes the Fermi level, which may be considered the highest energy level occupied by the electrons at 0 K; T the temperature and k_B is Boltzmann's constant.

Boltzmann identified three possible reasons for changes in the distribution function, namely diffusion, influence by external fields and collisions between electrons and lattice imperfections. The mathematical statement of these three assumptions give rise to the Boltzmann transport theory,

$$\frac{\partial f}{\partial t} = \left.\frac{\partial f}{\partial t}\right|_{diffusion} + \left.\frac{\partial f}{\partial t}\right|_{fields} + \left.\frac{\partial f}{\partial t}\right|_{coll}.$$

Substituting for the partial derivatives due to diffusion and fields, the Boltzmann transport equation reads

$$\frac{\partial f}{\partial t} + \mathbf{v} \cdot \nabla_{\mathbf{r}} f + \dot{\mathbf{k}} \cdot \nabla_{\mathbf{k}} f = \left.\frac{\partial f}{\partial t}\right|_{coll}.$$

where $\dot{\mathbf{k}}$ is determined by the external electric and magnetic fields, $\mathbf{E}$ and $\mathbf{B}$, by the relation

$$\hbar\dot{\mathbf{k}} = -e(\mathbf{E} + \frac{1}{c}\mathbf{v} \times \mathbf{B})$$

and the particle velocity is

$$\mathbf{v} = \frac{1}{\hbar}\nabla_{\mathbf{k}} E.$$

The collision term of the equation is expressed in terms of quantum mechanical scattering probabilities. How scattering probabilities are calculated will be elaborated in the next section. For now, we'll assume that the rate of transition per unit time from a state $\mathbf{k}$ to another state $\mathbf{k}'$ is given by $W(\mathbf{k}, \mathbf{k}')$. This particular scattering event can only happen if the state $\mathbf{k}$ is occupied and the state $\mathbf{k}'$ is free. The probability of $\mathbf{k}$ being occupied is

$f(\mathbf{k})$ and the probability that it is free is $(1 - f(\mathbf{k}))$. The total change in $f(\mathbf{k})$ is given by the difference between the increase due to scattering into the $\mathbf{k}$-state and the decrease due to scattering out of the $\mathbf{k}$-state. These two terms should be integrated over all $\mathbf{k}'$-states, the resulting collision term is thus expressed:

$$\left.\frac{\partial f}{\partial t}\right|_{coll} = \frac{1}{(2\pi)^3} \int \left[f(\mathbf{k}')(1 - f(\mathbf{k}))W(\mathbf{k}', \mathbf{k}) - f(\mathbf{k})(1 - f(\mathbf{k}'))W(\mathbf{k}, \mathbf{k}') \right] \mathrm{d}^3\mathbf{k}'.$$

2.5 Scattering events

In semi-classical transport models, the electron is considered to be of wave nature during the collisions with the lattice or interactions with other particles, these interactions are therefore referred to as scatterings. A scattering is a transition between two electronic states, the wave picture indicates a deflection of the wave.

In quantum mechanic theory, the transitions between electronic states are caused by imperfections in an otherwise perfect periodic lattice potential. Assuming that the deviations from the original potential are small, we may use perturbation theory , and the hamiltonian of the system may be written

$$\mathcal{H} = \mathcal{H}_0 + \mathcal{H}_j,$$

where $\mathcal{H}_0$ is the Hamiltonian of the unperturbed system and $\mathcal{H}_j$ is the perturbation causing the transition.

A general result derived using time dependent perturbation theory is the Fermi Golden rule. It states that the transition rate per unit time from an initial state $\mathbf{k}$ in band n to a state $\mathbf{k}'$ in band m is given by [5]:

$$\Gamma_j(n, \mathbf{k}; m, \mathbf{k}') = \frac{2\pi}{\hbar} \left| \langle m, \mathbf{k}' \mid \mathcal{H}_j(\mathbf{r}) \mid n, \mathbf{k} \rangle \right|^2 \delta(E_m(\mathbf{k}') - E_n(\mathbf{k}) \pm \hbar\omega),$$

where $\hbar\omega$ is the energy emitted (upper) or absorbed (lower) during the process. The Delta function ensures conservation of energy during the process. The total scattering rate per unit time for transitions out of the state $\mathbf{k}$ of band n is found by performing the summation over all states the system can transition into:

$$\Gamma_j(n, \mathbf{k}) = \frac{2\pi}{\hbar} \sum_{m,\mathbf{k}'} \left| \langle m, \mathbf{k}' \mid \mathcal{H}_j(\mathbf{r}) \mid n, \mathbf{k} \rangle \right|^2 \delta(E_m(\mathbf{k}') - E_n(\mathbf{k}) \pm \hbar\omega). \quad (2.2)$$

To obtain the scattering rates to be used in a Monte Carlo simulator, 2.2 is evaluated for specific scattering potentials, H_j. This is explained in [6].

2.6 Applying the theory to the particle simulator

So far this chapter has summed up some relevant topics found in text book theory of solid state physics and quantum mechanics. It is time to look at how this theory is applied in a Monte Carlo particle simulator.

The Monte Carlo method is based on the assumption that the Schrödinger equation has already been solved, and a model of the band structure is available either as an analytical expression or as a look-up table. This makes it is possible to assign an energy to a given momentum state. Full-band Monte Carlo models include accurate representations of the band structure, but are computationally more costly than simpler analytical models.

It is also assumed that the scattering rates of all the scattering processes which are considered relevant have been obtained in advance using the The Fermi Golden Rule. The rates are function of particle energy and should be available to the simulator as tables.

Summing up the Monte Carlo method in brief, we initialise each particle with a state consisting of its **k**-vector, position and valley or band. We then follow the trajectory of each particle by integrating up its momentum in time during the free flights. The particles are scattered at certain times according to the scattering rates; the scattering rates assure that a particle high in energy will have a high probability loosing energy in a scattering event while the opposite is true for a particle low in energy. After the simulation has run for some time, we end up with a statistical distribution of particles which is independent of the initial states. It can be shown that the distribution function obtained using this technique satisfies the Boltzmann's transport equation in he long time limit [5].

The energy bands and scattering rates are obtained from quantum mechanics where the wave picture of electrons is used, but in the Monte Carlo model, the electrons and holes are viewed as particles. This is the reason why the Monte Carlo method belongs to the category of semi-classical transport theories. The fact that the particles are simultaneously sharp in position and momentum poses a limit to the validity of the model because according to the uncertainty principle of quantum mechanics, these quantities cannot

be precisely determined at the same time. If we require the uncertainty in momentum to be much smaller than the average particle momentum and at the same time the uncertainty in position to be much smaller than the mean free path, Jacoboni [7] shows that the validity of the semi-classical theory is ensured when collisions are less frequent than 10^{14} s. Thus in case of high scattering rates, quantum transport theories should be employed rather than the Monte Carlo method.

Chapter 3

The Monte Carlo simulator

This chapter starts out with a brief description of the Monte Carlo simulator developed during the work with this thesis. The intention of section 3.1 is to give an overview of the simulator as a whole, including the parts that has not been changed during the work with this thesis. The following sections throughout this chapter will focus on the algorithms implemented in order to extend the Monte Carlo simulator from a bulk simulator to a device simulator. Section 3.2 sketches a the device geometries which has been implemented during the work with this thesis. Some changes have been made to the equations governing the electron dynamics within the device, these are presented in section 3.3. In order to solve Poisson's equation and obtain the electric field within the device, the positions of the mobile carriers needs to be converted to the format of a charge density matrix. The cloud in cell algorithm which has been implemented is described in section 3.4. The device has been made capable of exchanging particles with its surroundings through the implementation of ohmic contacts. The contact model and program implementation is described in section 3.5. Section 3.6 describes how the current running through the device is measured. A description of the particle boundary conditions at the edges of the device is given in section 3.7. Finally, sections 3.8 and 3.9 discuss the physical interpretation of superparticle charge and charge density when a 3D device is modelled in 2D.

3.1 Description of the program

The Monte Carlo simulator developed during the work with this thesis has been in development by students at the Norwegian Defence Research Establishment (FFI) since 2007. Earlier versions of the program are described in the Master's theses of Norum [8], Olsen [9] and Skåring [10]. The purpose of the student project at FFI is to develop a versatile tool for modelling materials and devices using both types of carriers. In addition to the simulations presented in the student theses referred to above, the program has been employed in simulations of laser pulse excitations in bulk material [11, 12].

The description of the program which will be given in the rest of this section follows the sequence elements in the program as they are presented in the pseudo code of figure 3.1.

The first task of the program is to present the user with a menu for setting simulation parameters. It allows the user to customise the simulation, selecting device or bulk simulation, device geometry, turning scattering mechanisms on and off, allowing the Pauli principle to be in action etc. The simulation parameters set by the user define which chunks of code will be executed during a simulation.

The next step is initialisation of the position and momenta of the electron and hole ensemble. The particles are initialised with randomised momenta drawn from a Maxwellian distribution. The initialisation of particle positions depends on the device to be simulated. The initial positions are drawn from a uniform distribution such that the device is initially charge neutral. When a simulation has run for a sufficiently long time, the particle distribution will be independent of the initial distribution [7]; however guessing an initial distribution close to the equilibrium distribution may shorten the simulation time required to reach equilibrium. The possibility of starting a simulation with the position and $\mathbf{k}$ distribution obtained at the end of a previous simulation has been implemented.

The scattering rates and energy band models determine when the scattering events will occur and the new particle states after scattering. The level of sophistication of a specific Monte Carlo simulator therefore relies heavily on the implementation of these two ingredients. The following scattering mechanisms are currently implemented in our model:

Carrier-carrier scattering
Coupled modes scattering

```
< Read user input from menu >
< Initialize simulation parameters >
< Initialize position and k-states of particles >
< Calculate scattering rates and energy tables>

for all timesteps
   < Perform carrier-carrier scattering >
   < Update charge density matrix >
   < Calculate electric field matrix >

   for all electrons
      < flight >
      < scatter >
   end

   for all holes
      < flight >
      < scatter >
   end

   < Inject / eject particles at contacts >
   < Measure current at the contacts >
   < Update hot phonons >
   < Update screening length >
   < Collect statistics >
end
```

Figure 3.1: Overview of the Monte Carlo simulator.

Polar optical scattering
Acoustic scattering
Ionised impurity scattering
Plasmon scattering
Non-polar scattering
Inter-valley scattering
Alloy scattering
Impact ionisation scattering

The scattering rates for most of these mechanisms have not been changed during the work with thesis. For a more thorough description of the rates, see [8, 9, 10] for descriptions and plots. The sources for most of the rates used with our simulator is [13, 14]. The impact ionisation scattering mechanism has been developed as part of this thesis, and will be described in section 7.4.

The program assumes a three-valley model for the conduction band. The electrons inhabit the Γ, L or X-valley. The conduction band model used is an analytical, isotropic and non-parabolic model. The program includes two hole bands, the heavy hole band and the light hole band which in the program are represented as tables [10].

The scattering rates and energy bands are fundamental elements of the Monte Carlo model. Details and plots of of the energy band of the Γ valley and the hole bands as well as the inter-valley and inter-band scattering rates are presented in the appendices A and B.

During simulation, the charge density matrix is updated using the cloud in cell algorithm and the electric field is calculated using the successive over-relaxation method every field adjusting time step.

Within the particle ensemble loops, the flight subroutine updates the particle positions. This routine first updates the particle momentum due to the electric field, then the new positions is found using time integration. The scatter subroutine determines the scattering rates for a particular particle depending on it's energy. The duration of the free flight is determined using random numbers; if a sufficient amount of time has passed since particle experienced its last scattering event, a new scattering will occur. A scattering mechanism is then chosen from the rates, which also includes self-scattering. The final **k**-state after scattering is computed in the local coordinate system where the z-axis is along the direction of the initial **k**-vector, and then trans-

formed to the global coordinate system of the device. If the Pauli principle is turned on, the particle will make a transition into the new state only if the state is unoccupied.

After the particle states have been updated, new particles may enter the simulation and existing particles may be evicted at the contact regions of the device. The screening length routine is described in [10] and the hot phonon routine in [8, 10].

At selected time steps, particle positions and **k**-vectors are among the simulation data which is written to file. Average particle energy, particle number and current measurement at the contacts are among the data written to file every simulation step.

3.2 Device geometry

Three different device structures have been simulated during the development and testing of the program. The n+ n n+ shown in figure 5.1 has been used for benchmarking the Monte Carlo program with respect to carrier mobilities and resistance. The *pn*-diode shown in figure 6.1 and the APD in figure 7.1 are simple components in which the *pn*-junction is the prominent feature.

We have chosen simple device geometries and fairly light doping densities in order to avoid complications during interpretation of the simulation results. The devices are easily modified in the user menu of the program.

3.3 Carrier dynamics

In the Monte Carlo simulator, the carrier dynamics is handled during the free flights. The existing flight routine in the Monte Carlo simulator has been updated to fit the $Cd_xHg_{1-x}Te$ material. Time integration of the particle momenta is used to compute the displacement of the particles during a simulation step, thus it is necessary to obtain the group velocity of the particles from the **k**-vector.

In general, the group velocity is related to the derivative of the energy:

$$\mathbf{v}_g = \frac{1}{\hbar}\nabla_{\mathbf{k}} E.$$

Models of the heavy and light hole bands and their derivatives were already incorporated into the program and are described in detail in [10]. The band model is isotropic, thus it depends on the modulus, k, rather than the $\mathbf{k}$-vector and thus the vectorial $\mathbf{v}_g$ cannot be obtained by differentiating the dispersion relation. In order to obtain the group velocity for the holes, we must introduce some approximations; inspired by [15], we choose the approximation

$$v_g = \frac{1}{\hbar}\frac{\mathrm{d}E}{\mathrm{d}k},$$

thus the derivative of the isotropic band is directly interpreted as the magnitude of the velocity. The hole velocity vector is then constructed using this quantity for the magnitude and the direction of the particle's $\mathbf{k}$-vector is directly adopted as the direction of the group velocity vector. Using this approach, the components of the group velocity of the holes are given by:

$$v_{g,i} = \frac{v_g}{k}k_i,$$

where $i \in (x, y, z)$.

The group velocity for electrons is found taking the derivative of the band structure, which is given in equation A.1, the result is:

$$v_{g,i} = \frac{\hbar k_i}{m^* \sqrt{1 + 4\alpha \frac{\hbar^2 k^2}{2m^*}}} \tag{3.1}$$

Here, $i \in (x, y, z)$, m^* is the effective mass at the bottom of the conduction band and α is the non-parabolicity parameter.

Once the velocity vector is obtained, the approximate displacement is found by [16]:

$$\Delta\mathbf{r} = \int_{t0}^{t1} \mathbf{v}_g(t')\mathrm{d}t' \approx \frac{1}{2}\left(\mathbf{v}_g(t_1) - \mathbf{v}_g(t_0)\right)\Delta t,$$

where t_0 is the time at the beginning of the flight, t_1 the time at the end and Δt the difference between these. The carrier dynamics for holes have not been changed during the work with this thesis.

3.4 Particle-mesh coupling

Particle-mesh coupling algorithms are designed to attribute the charge of stationary and mobile charges located at arbitrary positions, such as (x_k, y_k), in figure 3.2 to the nodes of a discrete charge density mesh.

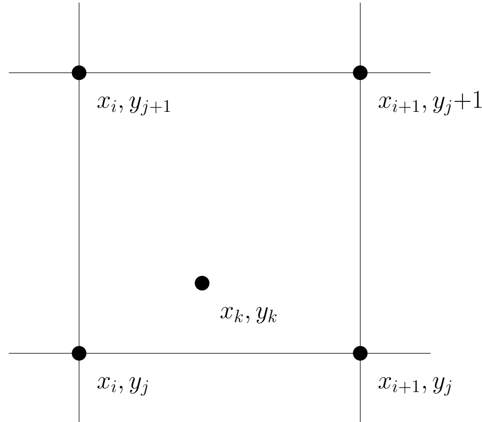

Figure 3.2: A particle positioned at (x_k, y_k), between the nodes of the computational mesh.

The simplest charge assignment method is the nearest grid point method (NGP). The charge of an electron at (x_k, y_k) in figure 3.2 is contributed to the nearest grid point, (x_i, y_j), such that the charge density it contributes to grid point (i, j) is:

$$\rho_{i,j} = \rho(x_i, y_j) = \frac{en\text{LxLy}}{N_s h_x h_y} = \rho_{sup}.$$

In this expression, e is the elementary charge, n the electron density, Lx and Ly the device lengths in the x and y-direction, h_x and h_y are the mesh spacing in the x and y-direction and N_s the number of superparticles participating in the simulation. ρ_{sup} is calculated at the beginning of a simulation, using the initial particle number in the device. The superparticle charge remains constant during simulation. The nearest grid point approximation is crude and results in a coarse and noisy approximation to the electrical potential.

A better method is the cloud in cell (CIC) method [17], which has been implemented in the Monte Carlo simulator during this work. This algorithm smears the charge density of the superparticle over its four nearest grid

points. The charge density in the mesh point with coordinates (x_i, y_j) due to the charge with coordinates (x_k, y_k) in the figure 3.3 is given by

$$\rho_{i,j} = \rho_{sup} \left(1 - \frac{|x_k - x_i|}{h_x}\right)\left(1 - \frac{|y_k - y_j|}{h_y}\right) \tag{3.2}$$

for $|x_k - x_i| < h_x$ and $|y_k - y_j| < h_y$ where h_x and h_y is the spacing between grid points. An important property of 3.2 is that the total charge contributed by the superparticles are conserved from the NGP scheme. This is easily verified; by adding the charge contributed by one particle to all of its four nearest nodes gives ρ_{sup}.

Instead of representing a point charge, as in the NGP scheme, the superparticle now represents a cloud of charge. This has a smoothing effect on the electrical potential computed in the Poisson solver. The cloud shape and the corresponding assignment function is visualised in figure 3.3.

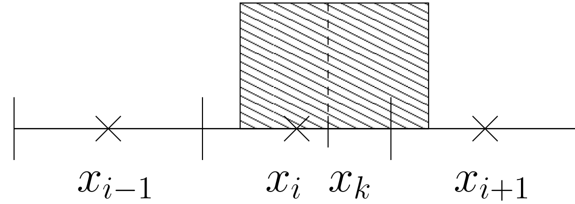

(a) Cloud shape

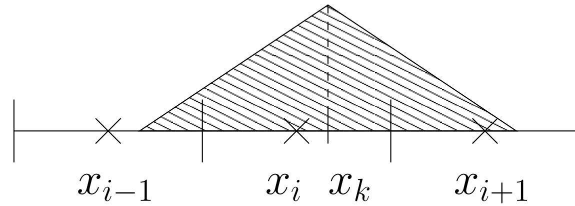

(b) Assignment function

Figure 3.3: The cloud shape and the assignment function for the Cloud in Cell algorithm. These figures are from Kim [14].

When Poisson's equation is solved, the potential and the electric field is obtained only in the nodes of the computational mesh. To evaluate the

electric field at the particle positions, a force interpolation scheme is needed. In this thesis, the NGP method has been used for this purpose while the CIC method has been employed to assign charges to the mesh.

3.5 Ohmic contacts

The contacts of a semiconductor device are semiconductor-metal interfaces where carriers can pass into or out of the device. There are two types of contacts, Schottky and ohmic contacts. In general, the metal and the semiconductor material have different work functions which creates a potential barrier for the carriers to surmount if they are to enter the device through a Schottky contact. An ohmic contact is a junction with no such barrier; it represents an ideal source or sink of carriers. The gate contact of a transistor is usually a Schottky contact while the source and drain contacts are ohmic.

The modelling of ohmic contacts poses one of the great challenges for device simulations. One reason is the complexity of the physics of the contact region where metal and semiconductor molecules form pockets of different alloy compositions [18]. Another reason is the fact that the contact implementation directly governs the number of particles entering and exiting the device, it thus directly controls the current through the device. Studying contacts is a research field of its own, and will not be the topic for this thesis. We will therefore be content with getting an overview of the most important contact models found in the literature, and choose one of the models that has been tested to yield reliable results and use it for our simulator.

There is a variety of contact models suggested in the literature, a classification of the different models can be found in [5], in which three main classes of models are identified. The first class is characterised by the two conditions of charge neutrality and thermal equilibrium in a small region adjacent to the contacts [19, 20, 18]. The charge neutrality condition is imposed to meet the zero voltage drop criterion. The model implemented in our simulator belongs to this class of models and it will be described in more detail below. Another class of models for two-terminal devices use periodic boundary conditions. A particle which is absorbed at one of the contacts gets re-injected at the opposite contact, either with the same wavevector that it was absorbed with or with a new wavevector randomly drawn from a thermal distribution. These models are considered unphysical [5]. This is due to the fact that the model simply does not reflect the real physics of the contacts. Yet another type of

model involves simulating the dynamics of the carriers in a reservoir adjacent to the device. An appropriate carrier distribution is obtained within the reservoir, and the dynamics of the reservoir determines the carrier injection into the device. This method is described in more detail in [20].

The first and the third class both agree with the understanding we have of the complex physics of the contacts. We have chosen to implement a model belonging to the first class because it is simple and presumably gives results which are easily interpreted. The contact model employed in our Monte Carlo simulator closely follows the approach of Fischetti and Laux which is described in [19].

The condition for injection is the charge neutrality condition of the contact region; if there is a net deficit of majority carriers, injection will happen until charge neutrality is maintained. The extension of the contact region into the device should be small, typically a few mesh cells [21, 16], as the number of injected particles may be affected by the choice. We have chosen $\mathrm{Ly}_{\mathrm{cr}} = 0.02$ μm for all devices and simulations. The contact region of the devices we have used for our simulations are shaded in the figures 5.1, 6.1 and 7.1.

The net charge in the contact region is calculated by counting free and immobile charges within the region, alternatively, it could have been calculated using the charge density matrix. If there is a net positive charge in the region, as many electrons needed to maintain charge neutrality are injected. The injected electrons are given a position vector drawn from a uniform distribution within the contact region. The thermal equilibrium condition is met by giving the injected particles a **k**-vector drawn from a thermal distribution. The half Maxwellian velocity distribution is used to ensure that the momenta of the injected particles are directed into the device. To improve the model, the displaced Maxwellian velocity distribution, which also takes into account the fact that the injected carriers are expected to have a drift velocity, should be implemented.

Absorption of a particle at the contact happens if the particle will hit the contact surface during the coming time step. Based on the current position and the group velocity, the estimated particle position at the next time step is calculated. If the new position falls at the contact surface or beyond it, the particle is absorbed and discarded from the simulation.

When simulating the *pn* junction and the APD structure, both electrons and holes are simulated at the same time. In this case, the contact on the *p*-side

injects only holes and the contact on the n-side injects only electrons. Both types of carriers are absorbed at both electrodes.

It should be noted that the charge per superparticle, which is discussed in more detail in section 3.9, is kept constant throughout the simulation, thus a device in operation is allowed to be electrically charged.

Contact regions are usually heavily doped, this has been taken into account in our model by introducing such zones beneath the contacts. Doing this smooths the transition between the metal contact and semiconductor device. However, the simulation of heavy doped contact region poses a problem to the Monte Carlo method because it requires the simulation of a relative large number of superparticles at the contact regions compared to the more lightly doped regions of the device. The carriers in the contact regions are far from the junction where carrier properties are most interesting, and they are often near thermal equilibrium. Simulating contact regions is computationally inefficient because a large number of superparticles needs to be simulated in order to obtain good statistics in the regions of low carrier density. A solution to this problem which may be implemented into our model in the future is offered by Mills *et al.* [22]. A charge enhancement factor is assigned to the superparticles in the low density regions such that once a particle enters this region, it is replicated a number of times corresponding to the charge enhancement factor. As a result, the same number of superparticles may be simulated, but with improved statistics at the regions of low carrier density.

An apparent weakness of the contact model implemented at present is that the source and drain contacts behave as separate sinks and sources of carriers, thus the model allows the charge continuity in the imagined circuit surrounding the device to be violated. The contact model should therefore be subject to further development; as a first approach, we suggest implementing the Ramo-Shockley particle boundary conditions [23].

Future development of the contact model should be fitted to the material properties of CMT, a detailed study of carrier transport and contact resistance in metal contacts of $Cd_xHg_{1-x}Te$ is presented in [24].

3.6 Measuring current

The current passing through the device is measured as the rate of carriers passing through the contacts of the device. The current is in general given

by

$$I(t) = \frac{\mathrm{d}Q(t)}{\mathrm{d}t},$$

for our devices, $Q(t)$ is the charge that has passed through an electrode up until the time t. It is given by

$$Q = q_s(N_a - N_i) + \varepsilon_s \varepsilon_0 \int \mathbf{E} \cdot \hat{\mathbf{n}} \mathrm{d}\sigma.$$

In this relation, N_i and N_a represents the number of particles injected or absorbed at the electrode up until the time t. The second term represents the displacement current; $\varepsilon_s \varepsilon_0$ is the electrical permittivity, $\hat{\mathbf{n}}$ is a normal vector to the contact surface and $\mathrm{d}\sigma$ a surface element. The integral is to be taken over the surface of the electrode. The contribution from the displacement term is negligible when the applied voltage bias is constant in time, but necessary when doing transient simulations.

We have defined the positive direction of the current into the device.

This method of measuring current is the most commonly employed method in Monte Carlo device simulations [5], but other methods exist. A method for measuring current at arbitrary crossections through the device is proposed in [25].

3.7 Boundary conditions

Boundary conditions enter the simulation at two stages, in the carrier dynamics and when solving Poisson's equation. The particle boundary conditions implemented in our simulator requires that when a carrier hits one of the edges of the device, it is specularly reflected. The boundary conditions of the Poisson solver are constant potential, known as Dirichlet boundary conditions, at the contacts, reflecting that external voltages are applied to the device under operating conditions. On the remaining edges, the equation is solved with von Neumann boundary conditions. The von Neumann conditions imply that no electric field can exist perpendicular to the edges of the device.

According to Jacoboni and Lugli [7], the source and drain voltages may be directly applied to the Dirichlet boundaries. Our simulation results indicate that this might not apply to non-symmetrical devices, this is discussed in section 6.2.

3.8 Modelling 3D devices in 2D

In the Monte Carlo simulator, a device is modelled in 2D by tracking the superparticles in all three dimensions of real space and momentum space, but Poisson's equation is solved only in 2D. This approach saves a considerable amount of computation time. A 2D model may sufficiently represent a real 3D device if the device has little variation in the direction perpendicular to the crossection we are simulating.

The physical interpretation of the superparticle charge and charge density in 2D is important to understand, and therefore deserves a discussion here. Poisson's equation in a 3D material reads

$$\nabla\left(\varepsilon_s \frac{\mathrm{d}\varphi}{\mathrm{d}\mathbf{r}}\right) = -\frac{\rho(\mathbf{r})}{\varepsilon_0},$$

where φ is the electrical potential. Assuming a constant relative permittivity, ε_s and no change in the z-direction, i.e. $\frac{\partial\varphi}{\partial z} = 0$, we are left with the 2D version of Poisson's equation,

$$\frac{\partial^2\varphi}{\partial x^2} + \frac{\partial^2\varphi}{\partial y^2} = -\frac{\rho(x,y)}{\varepsilon\varepsilon_0}$$

The unit of the charge density, ρ, remains the same in the two and three dimensional equation, namely Cm^{-3}. As a consequence, the charge of a superparticle in 2D should be interpreted as a charge per unit length in the perpendicular direction, and the corresponding charge density of two dimensional superparticles in an area should be interpreted as charge density per unit length in the perpendicular direction. The corresponding geometrical interpretation is that a superparticle represents a rod of charge [7].

3.9 Superparticles in 2D and 3D

In a device of typical size, the number of real conduction band electrons is far too large that every particle can be simulated. Instead, we employ the concept of superparticles. A superparticle may be interpreted as a statistical representation of a number of particles. The superparticle behaves as a single electron during the scattering events and is attributed the charge of a single electron moving in the electric during the free flights. However, when the charge density matrix is constructed for solving Poisson's equation, or when

the current through the device is measured, the charge of the superparticle is equal to the charge of the real particles that it represents.

The charge per superparticle is found by the principle that the total charge of all the superparticles should equal the total charge of all the real conduction band electrons in the device, thus the superparticle charge is

$$q_s = \frac{Q_{device}}{N_s} = \frac{enV}{N_{s,initial}}$$

where Q_{device} is the total charge of the conduction band electrons in a device and V is the three dimensional volume of the device. $N_{s,initial}$ represents the number of superparticles at the beginning of a simulation.

The use of superparticles makes the Monte Carlo device simulation feasible, but there are some disadvantages. The large charge of the superparticles magnify the natural fluctuations in the local electron density of the device, and thus causing larger fluctuations in the computed electric field than what is actually the case [21]. A particle that is accelerated in an artificially large field will achieve too high energy and thus the probability of scattering will be affected. It is therefore important for the validity of the simulation to use enough superparticles. According to our experience, the number of particles simulated with our devices should be at least ~ 50000 to avoid this effect.

Chapter 4

Poisson's equation

Using the Monte Carlo method is an efficient way to obtain the simultaneous solution of Boltzmann's transport equation and Poisson's equation. This approach is known as the self-consistent Monte Carlo model; it involves that Poisson's equation is solved every field adjusting time step during the simulation. A field adjusting time step corresponds to a few basic time steps of the Monte Carlo simulator. A single simulation requires Poisson's equation to be solved several thousand times, thus it is clear that a quick solver is needed.

In this chapter, we will first present Poisson's equation in section 4.1, the discrete formulation for our model problem is presented in sections 4.2 and the corresponding boundary conditions are presented in section 4.3. Tn section 4.4, we will have a brief look at some different numeric schemes which solve this problem and argue why our choice fell on the successive overrelaxation method. Finally, the Poisson solver implemented in our Monte Carlo simulator will be described in section 4.5.

4.1 Poisson's equation in a material

Poisson's equation is a stationary equation to obtain the electric potential, $\varphi(\mathbf{r})$, due to a given charge distribution $\rho(\mathbf{r})$. In a material, Poisson's equation is

$$\nabla\left(\varepsilon_s \frac{\mathrm{d}\varphi}{\mathrm{d}\mathbf{r}}\right) = -\frac{\rho}{\varepsilon_0}, \tag{4.1}$$

where ε_s is the dielectric constant for the material. In general ε_s is not a constant, but varies spatially, implying that the equation is non-linear. In our case, the linear approximation has been made. A thorough mathematical description and proof of existence of a unique solution can be found in [26].

4.2 The finite difference formulation

The finite difference formulation of the 2D Poisson's equation is obtained by discretising the equation on a uniform grid with $N = \mathrm{Nx} \times \mathrm{Ny}$ nodes, where Nx and Ny are the number of nodes in the x- and y-direction respectively. In principal, the spacing in x- and y-direction may be different. Here we'll assume equal spacing, h, implying that the coordinates of the nodes are $x_i = i \cdot (h-1)$, $i \in [1, Nx]$ and $y_j = j \cdot (h-1)$, $j \in [1, Ny]$.

The discretised Poisson's equation is obtained by approximating the second order partial derivatives using Taylor expansion. This is done in many text books, see for instance [26, 27]. The finite difference formulation of 4.1 on the uniform grid is

$$\frac{\varphi_{i+1,j} - 2\varphi_{i,j} + \varphi_{i-1,j}}{h^2} + \frac{\varphi_{i,j+1} - 2\varphi_{i,j} + \varphi_{i,j-1}}{h^2} = -\frac{\rho_{i,j}}{\varepsilon_s \varepsilon_0}, \tag{4.2}$$

where $\varphi_{i,j}$ denotes the potential in the mesh point (i, j). This approximation is called the five point difference approximation, it has an error $O(h^2)$ because the Taylor expansions are truncated after the h^2-term. The computational stencil for this approximation is illustrated in figure 4.2a.

The discretised Poisson's equation constitute a system of linear equations, one equation for each node in the grid. Re-indexing the nodes, $\varphi_{i,j} \to x_k$ where $k \in [1, N]$, the system of equations may be formulated as a matrix equation, $A\mathbf{x} = \mathbf{b}$. In this equation, the unknown potential in the nodes is contained in the $\mathbf{x}$ -vector, A is the coefficient matrix and $\mathbf{b}$ contains the source term and the boundary conditions.

The coefficient matrix of the five point stencil is the block diagonal matrix

$$A = \begin{bmatrix} T & -I & & & & \\ -I & T & -I & & & \\ & & & \ddots & & \\ & & & -I & T & -I \\ & & & & -I & T \end{bmatrix}, \tag{4.3}$$

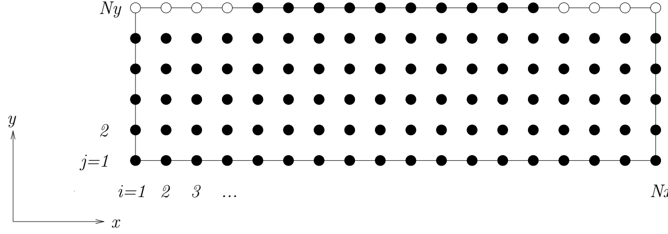

Figure 4.1: The computational mesh used for the solution of Poisson's equation. The value of the potential in the white nodes are set by Dirichlet boundary conditions.

where the $-I$-block is the negative identity matrix and

$$T = \begin{bmatrix} 4 & -1 & & & & & \\ -1 & 4 & -1 & & & & \\ & & & \ddots & & & \\ & & & & -1 & 4 & -1 \\ & & & & & -1 & 4 \end{bmatrix}. \tag{4.4}$$

After having solved the system of linear equations and obtained the electric potential, the electric field is found using centred difference:

$$Ex_{i,j} = -\frac{\varphi_{i+1,j} - \varphi_{i-1,j}}{2h}$$
$$Ey_{i,j} = -\frac{\varphi_{i,j+1} - \varphi_{i,j-1}}{2h}$$

4.3 Boundary conditions

The finite difference formulation of equation 4.2 described in the previous section is valid only for the interior nodes of the computational mesh. At the nodes representing the contacts, a constant electrical potential is imposed and thus the equations representing these nodes are simply eliminated from the system of equations. At the remaining edges, von Neumann boundary conditions are applied.

In order to apply the von Neumann boundary conditions, Taylor expansion is used to approximate the normal components of the first derivatives. At

the top and bottom edges of the device in figure 4.1, the normal component of the derivative is

$$\frac{\partial \varphi_{i,j}}{\partial y} \approx \frac{\varphi_{i,j+1} - \varphi_{i,j-1}}{2h}, \tag{4.5}$$

where $j = 1$ for the lower edge and $j = Ny$ for the upper edge. A corresponding equation is needed for the left and right edges. Forcing zero flux in equation 4.5 at the lower edge where $j = 1$, we get

$$\varphi_{i,0} = \varphi_{i,2}. \tag{4.6}$$

The point mesh node $(i, 0)$ lies outside the grid we have defined for our model problem; thus the von Neumann boundary conditions makes it necessary to introduce what is called ghost nodes. In these nodes, the value of the potential is known and given by equations similar to 4.6. The equation valid at the lower von Neumann edge of our problem is illustrated by the computational molecule in the second panel of figure 4.2.

The corner nodes requires special treatment because the normal direction to a corner is not well defined. The rectangular grid allows two normal directions at the corner nodes, the x- and the y-direction. Only one condition in each boundary node can be prescribed if the system is not to be overdetermined. According to [28], the analytic requirement

$$\int_c \frac{\partial \varphi}{\partial n} \mathrm{d}s = 0 \tag{4.7}$$

where c is the boundary curve and n the normal direction, must hold to ensure a unique solution. The stencil used for the corner nodes is shown in the third panel of figure 4.2 has been implemented to ensure that 4.7 will not be violated.

4.4 Overview of numerical methods

In the research field of Monte Carlo device simulation, a variety of different methods are in use for solving Poisson's equation. This reflects the fact that each method has its own strength which may be particularly useful when solving a specific problem. Future development of the Monte Carlo simulator should therefore include the incorporation of a set of solvers based on different solution methods.

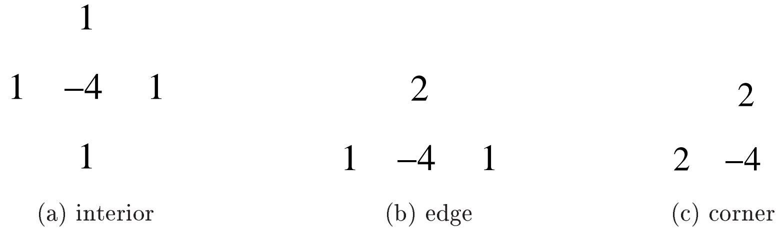

Figure 4.2: Computational stencils used for the A-matrix of the finite difference formulation of Poisson's equation. Panel (a) is valid for the equations corresponding to interior grid points, (b) for nodes the edges and (c) for the corner nodes.

.

Vasileska [5] argue that the Fast Multipole Method (FMM) is an efficient way of solving the 3D problem. In this method, multipole expansion is used to reduce the complexity of the Coloumbic many-body problem prior to force evaluation.

The finite element method (FEM) is another frequently used solver for Poisson's equation. This method allows a refined mesh in areas which require high resolution, such as the area surrounding localised impurities. For this reason, the FEM method is well suited for simulation of quantum structures.

For this thesis, we have chosen the successive over-relaxation method which belongs to the class of iterative solvers. The iterative solvers are flexible with respect to boundary conditions because few changes need to be made to the code in order to simulate different device geometries. Due to the nature of the self-consistent Monte Carlo method, an iterative solver is a good choice [29]; because the simulation time elapsed between two consecutive solutions is small, thus the solution obtained at the previous time step makes a good starting guess at the solution which is to be computed this time step. Furthermore, the successive overrelaxation method can be combined with the multigrid technique in advance of parallellising the code in order to further improve the solution time [5].

4.5 The relaxation methods

The relaxation methods offer a fast solution to Poisson's equation and are efficient in terms of storage [7]. The solution offered by iterative solvers is an approximate solution, the approximation is controlled by a chosen toler-

ance. The simplest of the relaxation methods is the Jacobi method which is described in detail in [27, 30]. The basic idea behind this algorithm and its successors; the Gauss-Seidel and the successive over-relaxation method with Chebyshev acceleration will be described in this section.

The relaxation methods are obtained by iterating equation 4.2. In the case of the Jacobi method, this is done straight forward:

$$\varphi_{i,j}^{(n)} = \frac{1}{4}\left[\varphi_{i+1,j}^{(n-1)} + \varphi_{i-1,j}^{(n-1)} + \varphi_{i,j+1}^{(n-1)} + \varphi_{i,j-1}^{(n-1)}\right] + \frac{h^2}{4}\frac{\rho_{i,j}}{\varepsilon_s\varepsilon_0}. \tag{4.8}$$

Here, n denotes the iteration number.

The first step of the Jacobi algorithm is to make an initial guess at the solution, $\varphi_{i,j}^{(0)}$, which is used as input on the right hand side of 4.8 to calculate a better guess $\varphi_{i,j}^{(1)}$. This procedure is repeated until the solution satisfies the criterion of convergence.

To have a closer look at the convergence of the Jacobi method, it is useful to go back to the matrix formulation of Poisson's problem. Splitting the A-matrix of 4.3 in two matrices, $A = D + R$, where D contains the diagonal elements of A and R contains all the off-diagonal elements, the equation can be rewritten:

$$\begin{aligned}(D+R)\mathbf{x} &= \mathbf{b}\\ \mathbf{x} &= -(D^{-1}R)\mathbf{x} + D^{-1}\mathbf{b}.\end{aligned}$$

The matrix $D^{-1}R$ is called the iteration matrix. The last equation is an implicit equation in $\mathbf{x}$ that can be iterated:

$$\mathbf{x}^{(n)} = -(D^{-1}R)\mathbf{x}^{(n-1)} + D^{-1}\mathbf{b}.$$

The convergence of the Jacobi method depends on the properties of the iteration matrix. The iterative methods are guaranteed to converge if the spectral radius of the iteration matrix satisfies

$$\rho_s(D^{-1}R) < 1.$$

The proof of this is given in [31]. The spectral radius of a matrix is the modulus of the largest eigenvalue of the matrix. For the coefficient matrix of the Poisson problem, it can be shown [30] that

$$\rho_s = \frac{\cos\left(\frac{\pi}{Nx}\right) + \cos\left(\frac{\pi}{Ny}\right)}{2}$$

for quadratic mesh cells. Each eigenvalue of the iteration matrix reflects the factor by which the amplitude of a particular eigenmode of undesired residual is suppressed during one iteration [30]. Proof is given in [32] that a diagonal dominant A-matrix ensures convergence of the Jacobi method.

The convergence rate for the Jacobi algorithm is slow, making it unsuitable for our purposes. However, there are several methods based on the simple idea of the Jacobi algorithm but with improvements to the convergence rate. The Gauss-Seidel method uses the latest information on the solution available. Assuming that the $\varphi_{i,j}$-values of an iteration are obtained in sequence, at the time $\varphi_{i,j}^{(n)}$ is calculated, $\varphi_{i-1,j}^{(n)}$ and $\varphi_{i,j-1}^{(n)}$ are already calculated and are available in the n-th iteration:

$$\varphi_{i,j}^{(n)} = \frac{1}{4}\left[\varphi_{i+1,j}^{(n-1)} + \varphi_{i-1,j}^{(n)} + \varphi_{i,j+1}^{(n-1)} + \varphi_{i,j-1}^{(n)}\right] + \frac{h^2}{4}\frac{\rho_{i,j}}{\varepsilon_s\varepsilon_0}. \tag{4.9}$$

The Gauss-Seidel method converges faster than the Jacobi method, though only marginally [7].

The successive overrelaxation method is an improvement to the Gauss-Seidel method. This method introduces an acceleration parameter, ω, to make an over-correction, anticipating corrections of future iterations. First, the Gauss-Seidel iterate, $\varphi_{i,j}^{GS(n)}$, is calculated using 4.9. The final n-th iterate is then calculated as the linear combination:

$$\varphi_{i,j}^{(n)} = \omega\varphi_{i,j}^{GS(n)} + (1-\omega)\varphi_{i,j}^{(n-1)}.$$

The relaxation parameter should take values in the range $1 \leq \omega \leq 2$. The convergence rate is optimised when [7]

$$\omega_{opt} = \frac{2}{1+\sqrt{1-\rho_s^2}}.$$

The convergence rate may be improved even further with a variable ω. This algorithm is called the cyclic Chebyshev method. It is similar to the successive over-relaxation method, but with

$$\begin{aligned}
\omega_0 &= 1 \\
\omega_1 &= \frac{1}{1-0.5\rho_s^2} \\
\omega_{p+1} &= \frac{1}{1-0.25\rho_s^2\omega_p}, \qquad p \geq 1.
\end{aligned}$$

4.6 Parallellising the Poisson solver

The successive overrelaxation method allows odd-even ordering of the mesh nodes. Calculating the potential in an odd point of the mesh requires only values of the potential in even nodes and vice versa. A half-sweep over the mesh updating all the odd mesh points is carried out before the second half-sweep which updates the potential in the even mesh points.

The possibility of odd-even ordering makes the Jacobi method and its successors inherently parallel. Using the checkerboard analogy, the even and odd mesh points may be compared to the black and white squares. The solution in all the black nodes may be calculated at the same time from the solution obtained at the previous iteration. Thereafter, the solution in all the white nodes may be calculated simultaneously from the knowledge of the solution in the black nodes of this iteration. This makes the class of methods described in section 4.5 very well suited for parallelisation.

Chapter 5

Accuracy and reliability of the model

In section 5.1 of this chapter, we present the general stability criteria for a Monte Carlo device simulation and assure that the simulation parameters we will use with later simulations obey them. The results of the simulator is tested in section 5.2 by studying the electron and hole mobilities obtained from bulk simulations. Finally, in section 5.3 we perform a simulation of a simple n+ n n+ structure in order to verify that our model is reliable.

5.1 Resolution in time and space

There are two types of stability criteria to consider when doing Monte Carlo simulations. On one hand, there are physical arguments which defines the resolution in time, Δt, and space, Δx. On the other hand there are numerical arguments which limit the coupling between the temporal and spatial resolution. A thorough discussion is presented in [33]. Here, we will check that the mesh cell size we have used for our Poisson solver, h; the basic time step, τ; and the field adjusting time step, τ_f, in our model satisfies the necessary criteria.

The mesh cells of the grid used for solving Poisson's equation should be small enough to resolve the smallest physical features relevant to the variation in the potential. The Debye screening length provides the characteristic length scale for variation in the electrical potential and carrier concentrations in

the Poisson-Boltzmann problem [34]. Thus it is natural to require that the mesh cell should be smaller than the Debye screening length, L_D. The Debye screening length is well approximated by the material parameter

$$L_D = \sqrt{\frac{\varepsilon k_B T}{n e^2}},$$

where $\varepsilon = \varepsilon_s \varepsilon_0$. In our model, the donor density of the heaviest doped regions are 1.0×10^{17} cm^{-3}, thus $h < 15$ nm. The devices we have simulated have a length of 3 µm, implying that the number of nodes in the x-direction, Nx, should be at least 200.

The physical argument limiting the basic time step, τ, is that we require all scattering events to be resolved. The most frequent scattering mechanisms have rates $\sim 10^{14}$ s^{-1}, thus we should have $\tau \leq 1$ fs.

The field adjusting time step, τ_f, determines how often Poisson's equation is solved. Some authors claim that the particles should not be allowed to travel across more than a few mesh cells during one field adjusting time step [21], while other [33] demand a mesh cell smaller than the longest distance travelled during a time step. In any case, the numerical requirement imposed on the relation between Δx and Δt can be expressed on the form:

$$v_{max} \Delta t < l_{max}, \tag{5.1}$$

where v_{max} is the maximal velocity component a particle can achieve during simulation. We have used $\tau_f = 5$ fs and measured the maximum velocity obtained during the simulations. By experience, this has produced stable simulations. The maximum velocity electrons reach in semiconductors in general is on the order 10^8 cm/s [33], thus the strictest interpretation of l_{max} in equation 5.1 requires a mesh cell 5 nm.

Yet another stability criterion for the relation between Δt and Δx which is often quoted in the context of device simulation is

$$\frac{\Delta t}{2} = \frac{1}{\omega_p}$$

where ω_p is the plasma frequency. However, in [35], it is argued that this applies to simulations of collision-less plasma rather than device simulations due to the stabilising effect of the scatterings.

5.2 Mobility

The mobility describes how strongly the particle motion is influenced by an applied electric field [36]. A carrier in an applied electric field will gain momentum and energy from the field, but the scatterings limit the achievable drift velocity. In the Monte Carlo simulator, the mobility provides an important check on the interaction between the band model, from which the particle velocity stems, and the frequency of the scatterings. The electron mobility is defined as the proportionality factor between the drift velocity and the electric field,

$$\mu_e = -\frac{v_d}{E_{ext}},$$

and likewise, the hole mobility is the proportionality factor between the drift velocity of the holes and the electric field. In CMT, the hole mobility is a few orders of magnitude lower than than the electron mobility due to the larger effective mass.

The electron and hole mobilities are extracted in bulk simulations where only one type of carrier participate in the simulation. Bulk simulations are used to eliminate undesired contact effects. The mobility is measured by applying a constant electric field and then the average drift velocity of the particles is measured after the Monte Carlo simulator has reached a stationary state. If the electric field is applied in the x-direction, the average drift velocity is measured as the average group velocity of the particles in the x-direction using equation 3.1. The drift velocity is averaged over the particle ensemble and over time.

The bulk simulations are performed at lattice temperature $T = 300$ K with a basic time step of 1 fs and an alloy fraction $x = 0.28$. The simulation results are presented in table 5.1.

E_{ext} in $\mathrm{kVcm^{-1}}$	μ_e in $\mathrm{cm^2V^{-1}s^{-1}}$	μ_h in $\mathrm{cm^2V^{-1}s^{-1}}$
0.1	1.82×10^4	117
0.3	1.77×10^4	137
0.5	1.78×10^4	148

Table 5.1: Electron and hole mobilities, μ_e and μ_h respectively, extracted from the Monte Carlo simulator at different applied electric fields, E_{ext}. The results were obtained at $T = 300$ K and $x = 0.28$.

There are considerable variations in the eperimentally obtained electron and hole mobilities [37]. The mobilities obtained by the Monte Carlo simulator are within range of the mobilities reported by the experimentalists, but they are in the lower end of it. We conclude that the values produced by the simulator appear reasonable. It should be noted that the Pauli principle was not taken into account during these simulations. As a consequences, some scatterings may have taken place that would else have been prevented by Pauli prohibition, and thus the extracted mobility may be artificially low.

5.3 Simulation of an n+ n n+ diode

In order to test the code and acquire experience on device simulation, the current voltage characteristics of a simple n+ n n+-device has been obtained. As a check, the resistance of this device has been compared to the ohmic resistance in a slab of CMT material which is similar in size to the simulated device.

The device simulated is sketched in figure 5.1, and the simulation parameters used is given in 5.2. The device is a symmetric n+ n n+ diode with three regions of different doping densities, the N_D region is relatively lightly doped compared to N_D^+ regions. The shaded regions of the device are the contact regions described in section 3.5. Only the electrons were simulated.

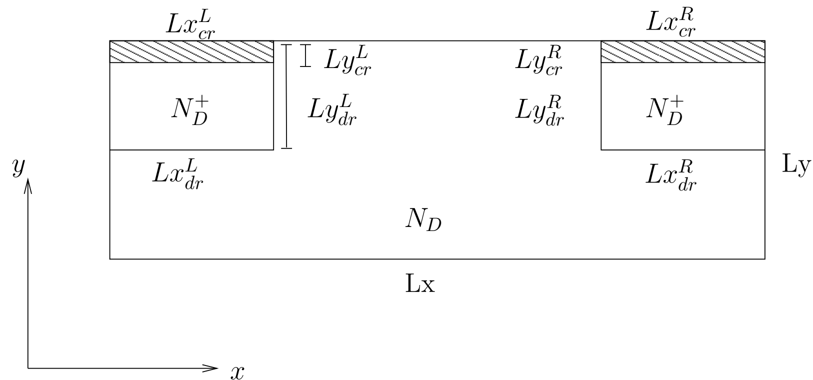

Figure 5.1: An illustration of the geometry of the n+ n n+ device. The shaded regions represent the contact regions.

The current-voltage characteristics of the n+ n n+-diode has been obtained by running simulations of the device under different bias voltages. The cur-

Lx	3.0 μm
Ly	1.0 μm
$\mathrm{Lx_{dr}}^L = \mathrm{Lx_{dr}}^R$	0.75 μm
$\mathrm{Ly_{dr}}^L = \mathrm{Ly_{dr}}^R$	0.50 μm
$\mathrm{Lx_{cr}}^L = \mathrm{Lx_{cr}}^R$	0.75 μm
$\mathrm{Ly_{cr}}^L = \mathrm{Ly_{cr}}^R$	0.02 μm
Nx	500
τ	1 fs
N_D^+	1×10^{17} cm^{-3}
N_D	1×10^{16} cm^{-3}
T	300 K
x	0.28

Table 5.2: Parameters for the n+ n n+ device. The symbols are explained in figure 5.1.

rent which runs through the device after the Monte Carlo simulation has reached equilibrium has been extracted averaging over a particle ensemble of ~ 50000 electrons and over 30 ps. The resulting IV-curve is shown in figure 5.2. The figure shows that at zero bias voltage, almost no current runs through the device while at higher voltages the current saturates, thus the component exhibits the behaviour of an n+ n n+-diode.

According to Ohm's law, the current running through a conductor is proportional to the voltage, thus the resistance is given by the slope of a linear IV curve. The n+ n n+-diode is a nonlinear component, but an approximation to ohmic resistance in the near linear region of the IV curve may be obtained from figure 5.2. The slope of region close to zero bias voltage is approximately 0.3 kΩ.

The formula used to calculate the Ohmic resistance in a slab of CMT material is

$$R = \rho \frac{L}{A}, \tag{5.2}$$

where L is the length of the slab in the direction of the current and A the crossection area. The resistivity, ρ is here considered a material parameter obtained via the electron mobility using the relation

$$\rho = \frac{1}{\sigma} = \frac{1}{e(n\mu_e + p\mu_h)},$$

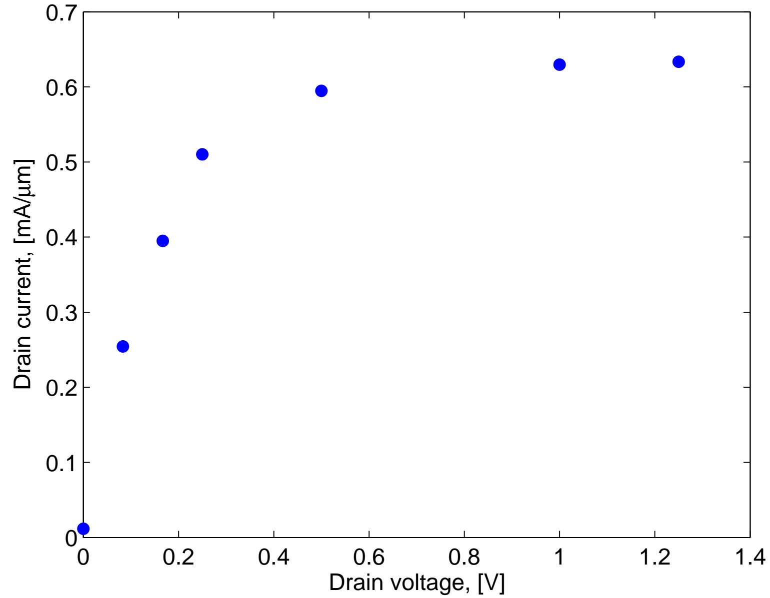

Figure 5.2: IV-curve of the n+ n n+ device.

where σ is the conductivity and p the hole concentration. We assume no contribution from the second term of the denominator, since the device is n type. We use an electron mobility value which is independent from our simulation results, in [38], $\mu_e = 3.5 \times 10^3$ cm^{2}V^{-1}s^{-1} is reported for CMT with a free electron concentration of 2×10^{15} cm^{-3}. This gives the resistivity $\rho = 5.49 \times 10^{-4}$ Ωm, corresponding to the resistance $R = 1.647$ kΩ for a slab which is 3.0 µm long with a crossection of 1 µm^2.

The discrepancy between the theoretically calculated resistance and the resistance measured in our program is within an order of magnitude. The resistance of the simulated device is smaller than the resistance through the slab, which contradicts our understanding that the contact regions would induce extra resistance compared to the slab. The contact regions of our device are however large compared to the device, the high doping density in these areas contribute to a lower resistance.

From the results presented in the last two sections, we conclude that that the model may need some fine tuning before it is used for more realistic simulations.

Chapter 6

PN junction

The Monte Carlo method is rarely used for studying simple *pn*-diodes. These structures may seem too simple to engage advanced simulation techniques such as the Monte Carlo method. Instead, simple analytic theories which are based on numerous simplifications are used. Apart from the studies Moglestue conducted in the 1980's [18, 39], Monte Carlo studies of *pn*-diodes are scarce.

Precisely because the *pn*-diode is described by analytic theory, this structure serves well as a starting point for discussion of the Monte Carlo method itself.

In this chapter, we have simulated a *pn*-device under reverse and forward bias voltage. The simulation parameters are presented in section 6.1 while the simulation results are presented in section 6.2 and 6.3 respectively. The results show that our Monte Carlo model is in qualitative agreement with the analytical *pn*-junction model. The current-voltage characteristics, or IV curve, has been obtained and is presented in 6.4 while the switching time has been studied in section 6.5.

6.1 Simulation parameters and assumptions

The *pn*-junction simulated has the geometry shown in figure 6.1, and the simulation parameters used are listed in table 6.2. The donor and acceptor densities at the junction, N_D and N_A have been set to 10^{16} cm^{-3} while the regions close to the contacts are more heavily doped, N_D^+ and N_A^+ have been set to 10^{17} cm^{-3}. The doping densities have been chosen fairly light

in order to make the approximation of neglecting the Pauli principle. The three simulations differ only in the Dirichlet boundary conditions imposed at the contacts of the Poisson solver. The voltages set at the left and right contacts are designated V_L, and V_R respectively; in table 6.1, the Dirichlet boundary conditions for the three simulations are given.

Type of external bias voltage	$V^L_{Poisson}$	$V^R_{Poisson}$
Near unbiased	-0.35	0.00
Forward bias	-0.10	0.00
Reverse bias	-0.60	0.00

Table 6.1: Overview of the boundary conditions used for the stationary *pn*-diode simulations.

The simulations have been performed assuming no generation or recombination of carriers. In [18], it is argued that the carrier lifetimes in GaAs are too long for a significant number of recombination events to take place, thus modelling recombination will have little effect on the simulation results. We consider the same argument to apply for our CMT diode.

It should also be mentioned that the simulations performed here were initialised with particle states consistent with the steady state of the Monte Carlo simulator at the given voltage. These states were obtained running transient simulations, starting from a qualified guess at the end states, until the Monte Carlo simulator reached its equilibrium. The Monte Carlo equilibrium for the stationary simulations was simulated for 100 ps.

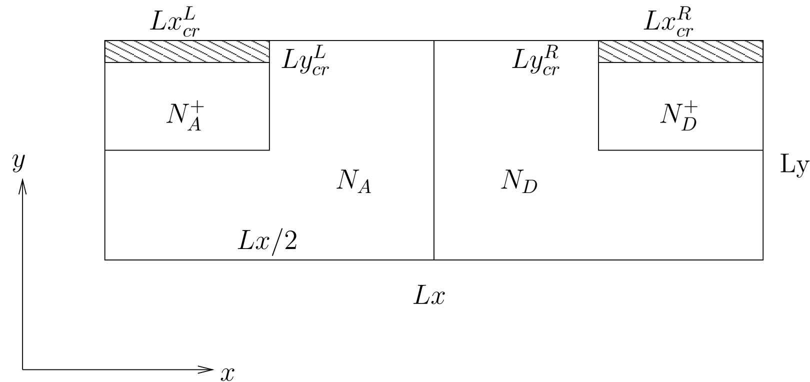

Figure 6.1: The geometry of the *pn*-diode. The shaded regions represent the contact regions.

Lx	3.0 µm
Ly	1.0 µm
${\mathrm{Lx_{dr}}}^L = {\mathrm{Lx_{dr}}}^R$	0.75 µm
${\mathrm{Ly_{dr}}}^L = {\mathrm{Ly_{dr}}}^R$	0.50 µm
${\mathrm{Lx_{cr}}}^L = {\mathrm{Lx_{cr}}}^R$	0.75 µm
${\mathrm{Ly_{cr}}}^L = {\mathrm{Ly_{cr}}}^R$	0.02 µm
Nx	600
τ	1 fs
N_D	1×10^{16} cm^{-3}
N_D^+	1×10^{17} cm^{-3}
N_A	1×10^{16} cm^{-3}
N_A^+	1×10^{17} cm^{-3}
T	300 K
x	0.28

Table 6.2: Simulation parameters used for the *pn*-diode simulations. The symbols refer to figure 6.1.

6.2 Simulation results under reverse bias

We know from standard text book theory, e.g. Tonning [40], that when *p*-type and *n*-type semiconductor material are put together to form a *pn*-junction, the holes close to the junction will diffuse from the *p*-side over to the *n*-side and likewise electrons will diffuse from the *n* to the *p*-side. On both sides of the junction, regions of uncompensated immobile charge are left, causing an electric field directed from the *n*-side towards the *p*-side. While the concentration gradient drives the diffusion process pushing the carriers past the junction, the electric field acts to draw the carriers back. In equilibrium, the drift and diffusion processes perfectly balances each other, the resulting electron and hole currents are zero separately.

Applying a more negative voltage to the *p*-side reinforces the electrostatic potential difference and hence the electric field across the junction, thus enhancing the drift current compared to the diffusion current. As a result, the extension of the depletion region will increase.

We have used the Monte Carlo simulator to simulate the carrier distribution and the depletion region of the *pn*-diode at operating conditions near equilibrium and under reverse bias. The resulting spatial distribution of carriers in the device in figures 6.2 and 6.3. The figures show that in both cases, a

depletion region arise at the junction and the depletion region is wider under heavier bias.

The width of the depletion region may be calculated analytically for a simple 1D junction. Tonning does this by solving Poisson's equation under the assumption that the depletion region is completely free of mobile carriers; the only contribution to the charge density is the acceptor density at the p-side and donor density at the n-side. The extension on the n-side is then given by

$$x_{N,eq} = \sqrt{\frac{2\varepsilon}{eN_D}\frac{N_A}{N_A + N_D}}\sqrt{\frac{kT}{e}\ln\frac{N_A N_D}{n_i^2}}, \tag{6.1}$$

and a similar expression is given for the extension at the p-side. The calculation is based on the assumption of drift-diffusion balance, which introduces the intrinsic carrier density, n_i. This quantity is not present in our Monte Carlo model, thus in order to do an informal comparison between our result and the analytical model, we have regarded the intrinsic carrier density a material constant that can be looked up in a table. In [37] a value of $n_i = 4.1 \times 10^{15}$ cm^{-3} is reported, using this with the formula above gives the dotted lines sketched into the carrier distribution plots. According to figure 6.9, it is clear that there are also two minor built-in voltage barriers on the border of the two heavier doped contact regions. Their existence may affect the potential barrier across the main junction, and thus there are several reasons not to take the comparison between the analytical model and our Monte Carlo model too seriously.

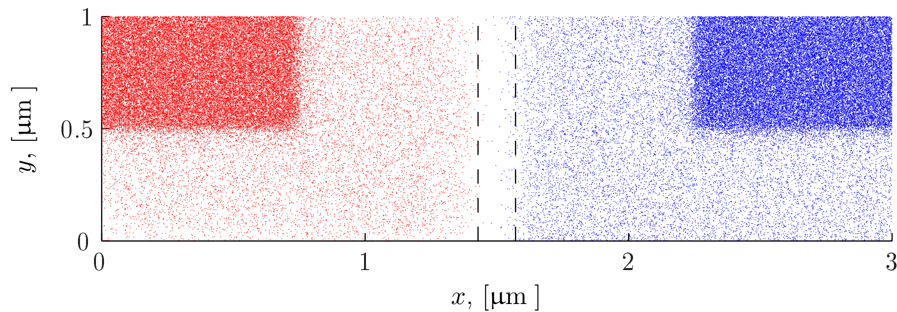

Figure 6.2: Spatial distribution of electron (blue) and hole (red) positions of the near unbiased pn-diode. The drawn lines correspond to the theoretical extension of the depletion region under zero bias voltage as calculated in [40].

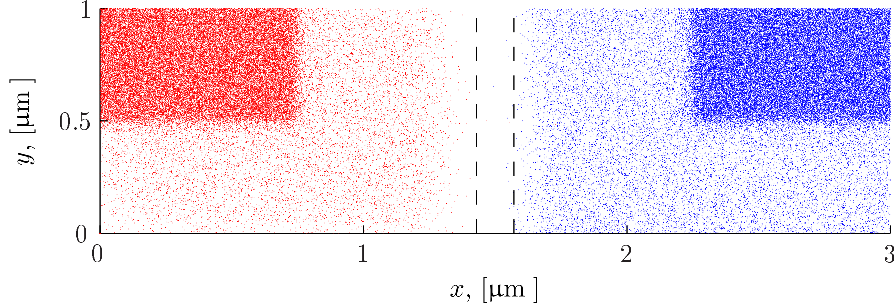

Figure 6.3: Spatial distribution of electron (blue) and hole (red) positions of the reverse biased pn-diode. The drawn lines correspond to the analytically calculated extension of the depletion region when the device is in equilibrium, i.e. zero bias voltage is applied.

The figures 6.4 and 6.5 give the quantitative picture of the carrier densities along the x-axis. The figures are obtained from the carrier positions; dividing the x-axis into bins of 60 nm and averaging out the y-direction.

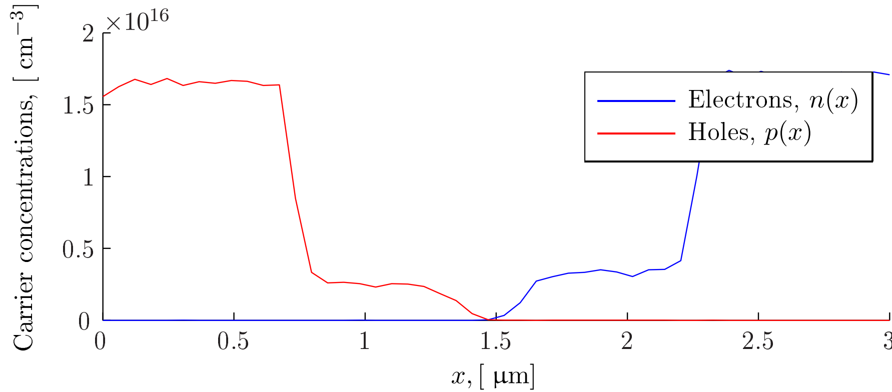

Figure 6.4: The concentration of holes (red) and electrons (blue) along the x-axis of the near unbiased pn-diode.

Representing the current running through the device as a function of time directly gives a picture which is dominated by statistical noise. We find it easier for the eye to capture what is actually going on by representing the cumulative charge that has passed through the contacts on the p and n-side during the simulation time. The figures 6.6 and 6.7 show this for the diode close to equilibrium and the diode under reverse bias respectively. The fact

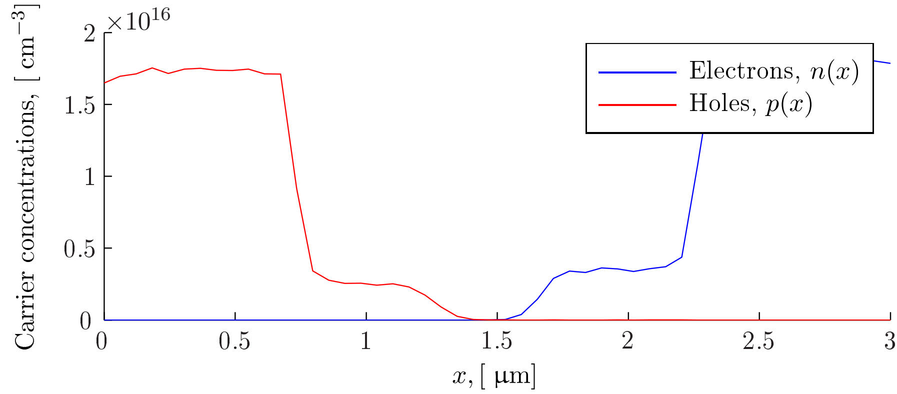

Figure 6.5: The concentration of holes (red) and electrons (blue) along the x-axis of the reverse biased pn-diode.

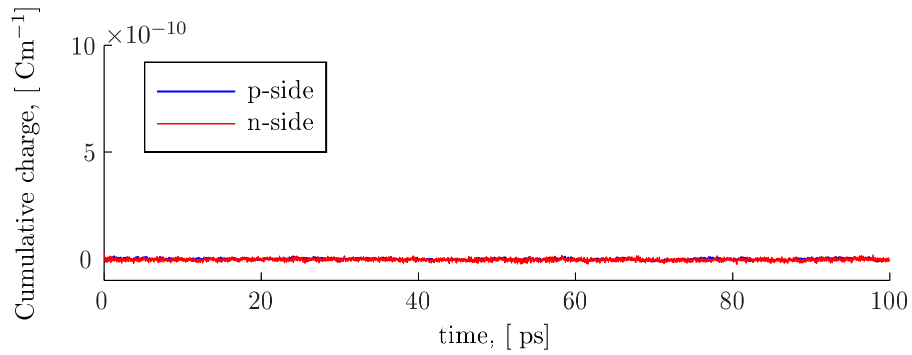

Figure 6.6: Cumulative charge that has entered the left contact and exited the right contact of the near unbiased pn-diode during the simulation.

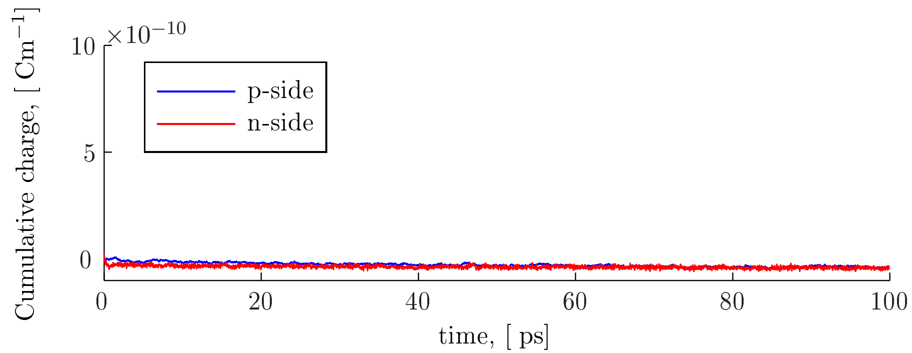

Figure 6.7: Cumulative charge that has entered the left contact and exited the right contact of the reverse biased pn-diode during the simulation.

that the curves are running parallel indicate that there is no accumulation of charge inside the device. The sign of the slope of the curve gives the direction of the current; positive slope indicates current in the forward direction of the diode, current in the reverse direction has a negative slope. The steepness of the slope indicates the amount of current running through the device.

Figure 6.6 indicate that almost no current runs through the device under weak reverse bias, while the plot in figure 6.7 has a very weak negative slope indicating a small current in the reverse direction. The current through a reverse biased diode is known to be mainly due to generation of electron-hole pairs in the depletion region. The generated carriers are swept in each direction by the electric field causing a small current. The generation process is not modelled in our particle simulator, thus the observation must correspond to noise.

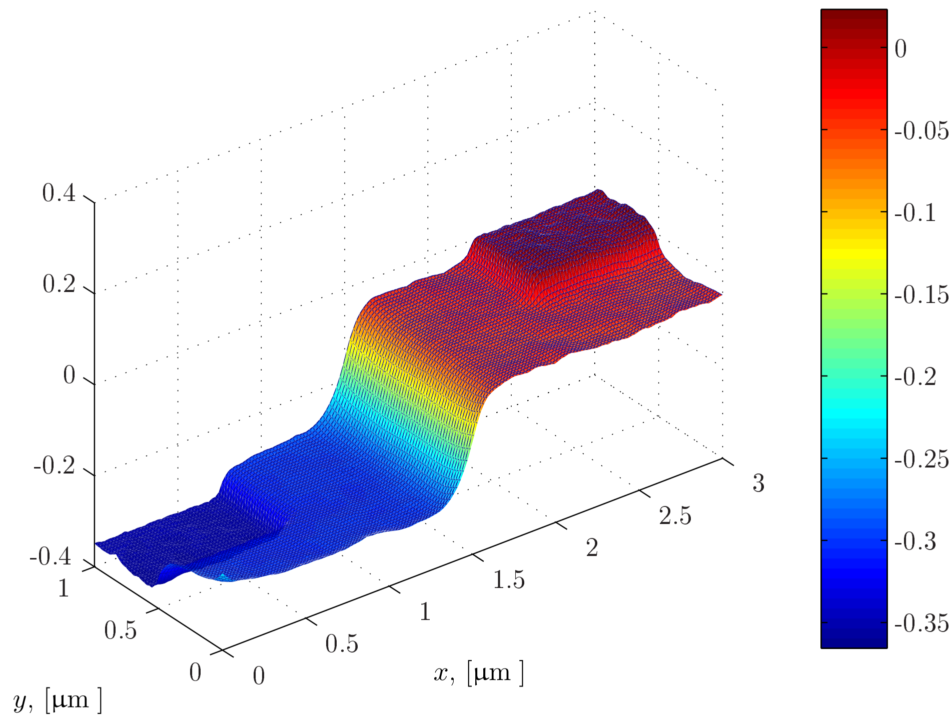

Figure 6.8: Electric potential in V in the near unbiased pn-diode. The p-side is to the left in the figure.

The 1D model which may be solved analytically gives an expression for the

built-in voltage across the junction:

$$V_{bi} = \sqrt{\frac{kT}{e} \ln \frac{N_A N_D}{n_i^2}}, \tag{6.2}$$

which would correspond to 0.2 V for a 1D CMT junction.

Figure 6.8 shows the electric potential, as it is computed by the Poisson solver, when the device is close to equilibrium. The potential difference across the device is approximately 0.35 V, which is somewhat larger than the potential predicted by the analytical model.

There are significant differences between the 1D junction and our simulated device that cause this difference; the simulated device contains two contact regions. Figure 6.9 show that there are three electric fields pointing in the same direction which together contribute to the 0.35 V we observe; thus it is appropriate that we observe a value which is larger than the analytically obtained result.

According to [7], the external bias voltage may be directly imposed as Dirichlet boundary conditions. We suggest that this may be true for symmetrical devices, but not necessarily for asymmetric devices such as the *pn*-diode. We observe that we need to impose a voltage difference of $0.2 - 0.3$ V between the contacts in order to simulate the device in equilibrium. This is related to the asymmetry of the *pn*-device. Wurfel [41] discusses the potentials which arise at a *p*-*n* junction in detail. There is a chemical potential difference at the junction due to the large concentration of holes on the *p*-side and electrons on the *n*-side. The chemical potential is exactly balanced by the built-in potential which is a purely electrical potential. The electrical potential causes an electric field from the *n*-side to the *p*-side; this field cannot perform any physical work and as a consequence no current can run in a circuit consisting of an unbiased *p*-*n* diode. This is evident because there is no source of energy in such a circuit. A voltmeter cannot measure a purely electrical potential, instead it measures the combined electrochemical potential difference; there is no deflection on the voltmeter in the circuit consisting of a *pn*-diode with no applied bias.

The Poisson solver sees both the built-in potential at the junction and the voltage difference imposed at the contacts. As a consequence, there is an offset between what we think of as an externally applied bias voltage and the Dirichlet boundary conditions.

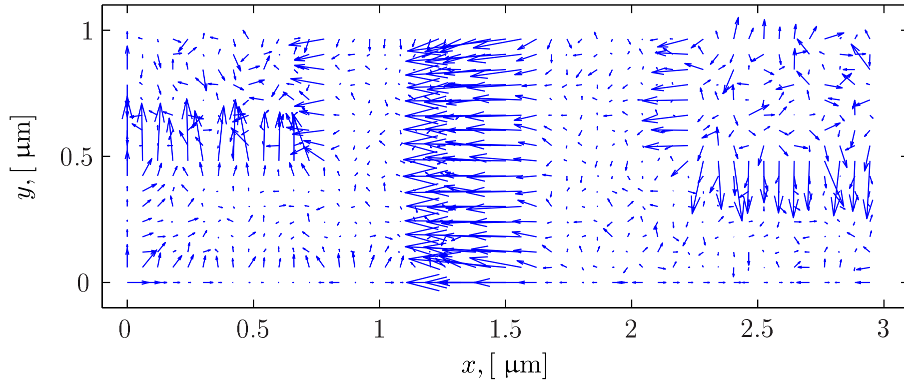

Figure 6.9: Electric field in the near unbiased pn-junction. The p-side is to the left in the figure.

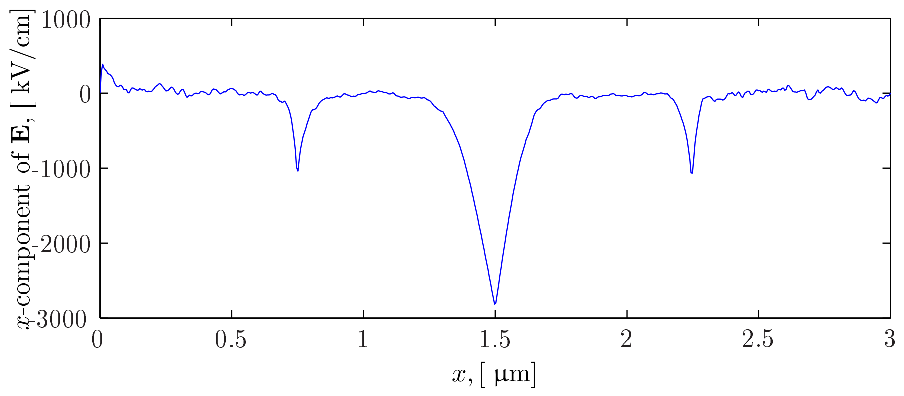

Figure 6.10: Electric field in the x-direction of the near unbiased pn-junction. The p-side is to the left in the figure.

The figures 6.9 and 6.10 show the electric field in the device when it is in equilibrium. The direction of the field is consistent with the analytical theory, it is directed from the n-side towards the p-side. There are also fields which indicate that smaller junctions arise at the contact region boundaries.

The field arising at the junction is large enough that, for future development of the simulator, it should be considered to take into account intracollisional field effects.

6.3 Simulation results under forward bias voltage

The device is forward biased by applying a positive voltage to the p-side relative to the n-side. This will lower the electrostatic potential across the junction and hence the drift-diffusion balance will be disturbed. The diffusion current is enhanced compared to the drift current, and thus the width of the depletion region is reduced. The figures 6.11 and 6.12 shows our simulation result of the carrier distribution in a forward biased pn-junction. The figures show that, compared to the unbiased case, the depletion region is decreased in extension.

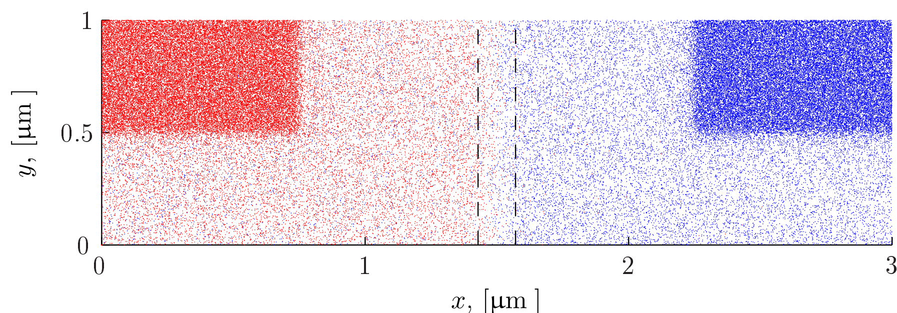

Figure 6.11: Spatial distribution of electron (blue) and hole (red) positions in the forward biased pn-diode. The drawn lines correspond to the analytically calculated extension of the depletion region when the device is in equilibrium.

The positive slope of the graph in figure 6.13 indicate that under forward bias voltage, there is a current running through the device from the p-side towards the n-side. Thus the qualitative result produced by our Monte Carlo model is consistent with the analytical model.

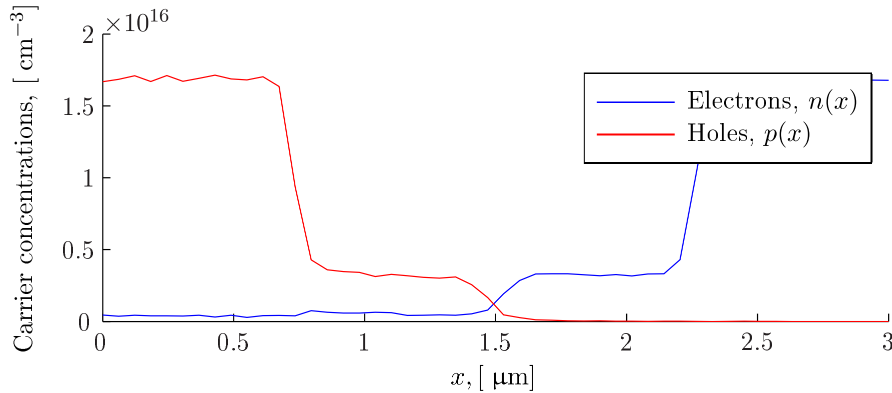

Figure 6.12: The concentration of holes (red) and electrons (blue) along the x-axis of the forward biased pn-diode.

The current found when taking the derivative of this curve is 1.0×10^{-2} mA/μm in the z-direction.

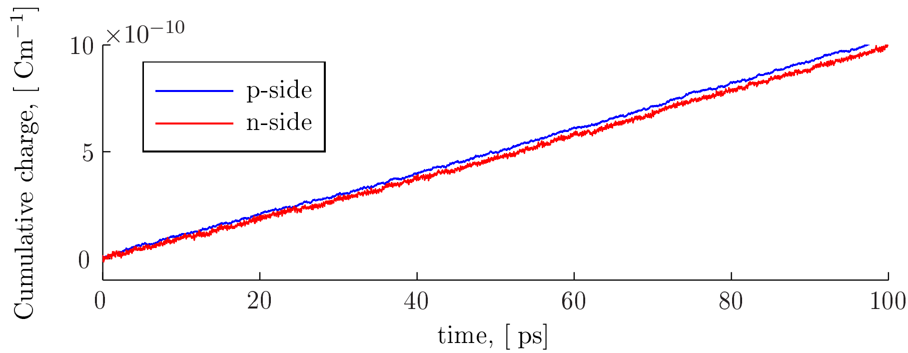

Figure 6.13: Cumulative charge that has entered the left contact and exited the right contact of the forward biased pn-diode during the simulation time of the forward biased pn-junction.

A similar study of a GaAs pn-device under forward bias has been conducted by Moglestue [18, 39]. In this study, Boltzmann's transport equation and Poisson's equation were solved self-consistently using the Monte Carlo method. The device had ohmic contacts in both ends. Moglestue observed the formation of an electron hole plasma at both sides of the junction; and he refers to experiments in which the luminescence from such a plasma has been measured. The density of the plasma reached four times the acceptor or donor density at the junction. Our results indicate that for a $Cd_{0.28}Hg_{0.72}Te$

diode under forward bias, there is a small accumulation of electron plasma at the p-side of the junction. This can be seen in both figure 6.12 and 6.11 if studied carefully. The effect may be due to the small effective mass of the electrons. The plasma effect observed for the CMT diode is much weaker than Moglestue's result indicate for the GaAs junction.

6.4 IV characteristics of the pn junction

The IV-characteristics for the pn-junction has been obtained running stationary simulations with varying $V_{Poisson}$ while measuring the current through the diode. The result is presented in figure 6.14. The figure shows that the pn-junction has the rectifying behaviour of a diode.

The current running through the diode under the three different operating conditions discussed in the previous sections is presented in table 6.3.

The IV curve shows that for our simulation results, there is no reverse leakage current in the diode. Reverse leakage current, or dark current in the context of photodiodes, is an undesired effect occurring in APD detectors which is due to generation of carriers in the depletion region of a reverse biased device. Dark current can in principle be studied using the Monte Carlo method, this requires the implementation of carrier generation rates obtained from first principles of quantum mechanics. However, due to the very low generation rate compared to the time step of the Monte Carlo method, the technique is inefficient in this respect. Several studies have been conducted on dark current in HgCdTe APDs [42, 43], in these studies, the transport equations have been solved using other methods than the Monte Carlo.

Type of external bias voltage	Total current at p-contact [mA/µm]
Forward bias	1.0×10^{-2}
Unbiased	-1.6×10^{-6}
Reverse bias	-3.5×10^{-4}

Table 6.3: Current running through the pn-diode during the three stationary simulations presented in the two previous sections .

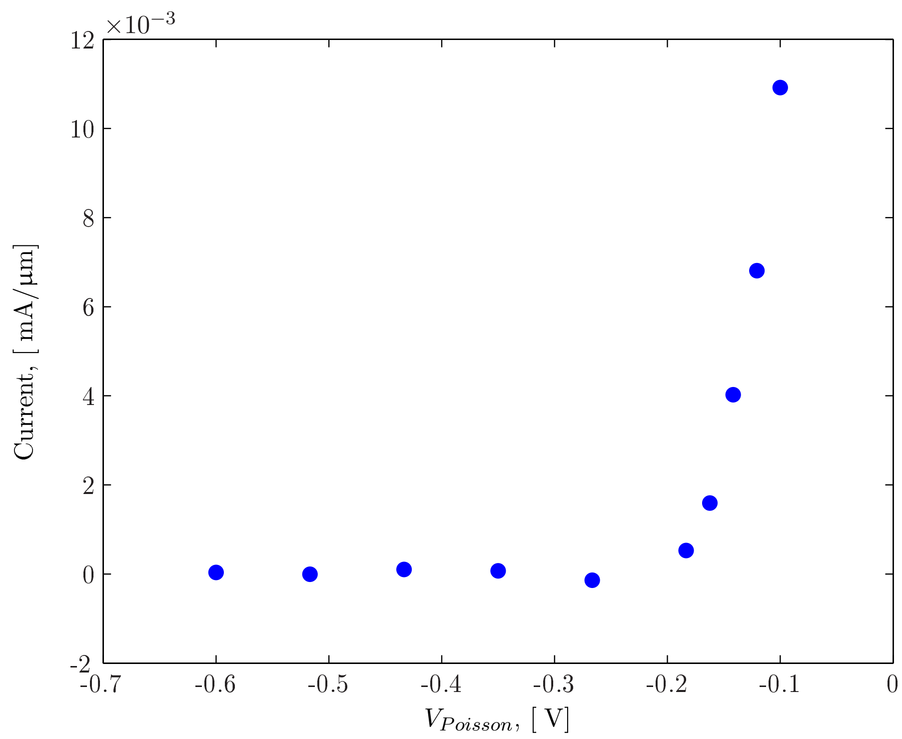

Figure 6.14: Current voltage characteristics of the *pn*-diode. $V_{Poisson}$ refers to the voltage difference at the Dirichlet boundaries of the Poisson solver.

6.5 Switching behaviour of a diode

The simulations described above are stationary simulations performed with constant voltage being applied to the diode. The Monte Carlo simulator is also suited for studying the transient dynamics. We have studied the behaviour of a diode which is switched from the current conducting to the non-conducting state.

Figure 6.15 shows a circuit where a diode is forward biased when the switch is in position 1 and reverse biased when it is in position 2. Assume that the switch was in position 1 at $t < 0$, and switched to position 2 at $t = 0$. The current through the diode and the voltage across it is sketched schematically as a figure of time in figure 6.16. Tonning's analysis of the switching process is the following: At $t < 0$, the diode is carrying a current in the forward direction. At $t = 0$ it starts carrying a large current in the reverse direction. This current is due to holes being pulled out from the n-side and electrons being pulled from the p-side. We term the time it takes for a diode initially in the on-state to switch to the off-state the *switching time*. At the time when the minority carrier concentrations near the depletion region has fallen off to the respective equilibrium levels, the current stabilises at the saturation current I_s, which runs in the reverse direction. This current is due to the generation of electron hole pairs in the depletion region. When $t \to \infty$, the voltage has reached the reverse bias, and thus the diode represents a large resistance in the circuit.

We have simulated the transient behaviour of the switching process and measured the switching time of the pn-diode for a reverse bias voltage of 5 V. The simulation was initialised with particle positions and momenta obtained after simulating the diode under forward voltage bias, i.e. $V_L = V_R = 0.0$. We used $V_L = -5.0$ and $V_R = 0.0$ as boundary conditions to the Poisson solver and otherwise the same simulation parameters as presented above. According to figure 6.17b there is a small reverse-current effect at the beginning of the simulation, but it is not as pronounced as Tonning's analysis suggest. Figure 6.17a shows that the current through the contacts drops off steadily and reaches a stationary level near zero. From figure 6.17 it is clear that after approximately $60 - 70$ ps, there is no current running through the device, and this is how we determine the switching time of the diode.

Figure 6.17b also reflects the fact that the charge of the diode changes under operation. This may be related to the particle boundary conditions at the

contacts. Modelling the *pn*-diode may require that the Ramo-Shockley particle boundary conditions [23] are implemented in order to better maintain charge continuity.

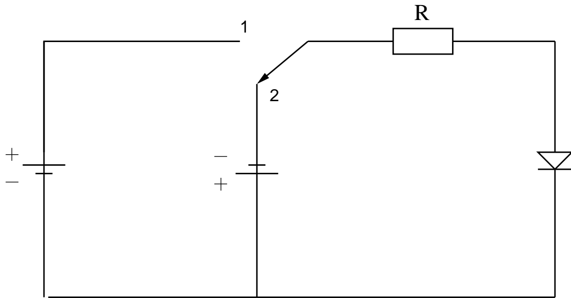

Figure 6.15: Circuit used for switching a diode between the conducting and non-conducting states. The figure is from [40].

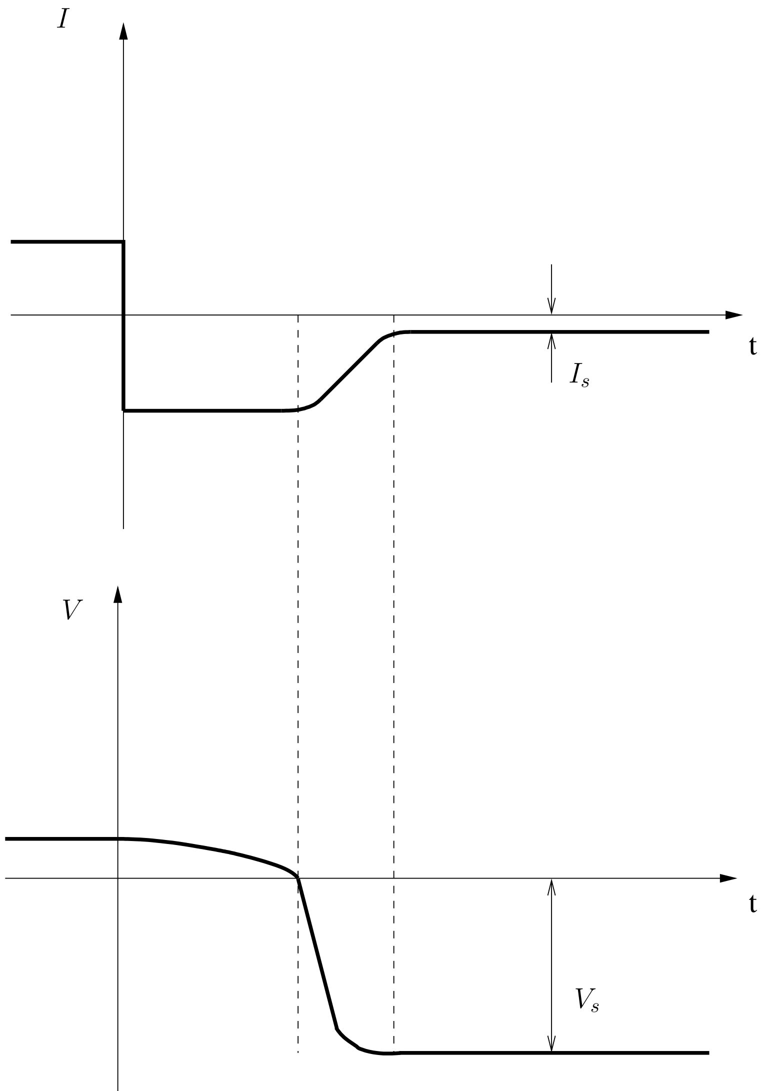

Figure 6.16: The current through and voltage over a diode which is being switched from the conducting to the non-conducting state at $t = 0$. The figure is from [40].

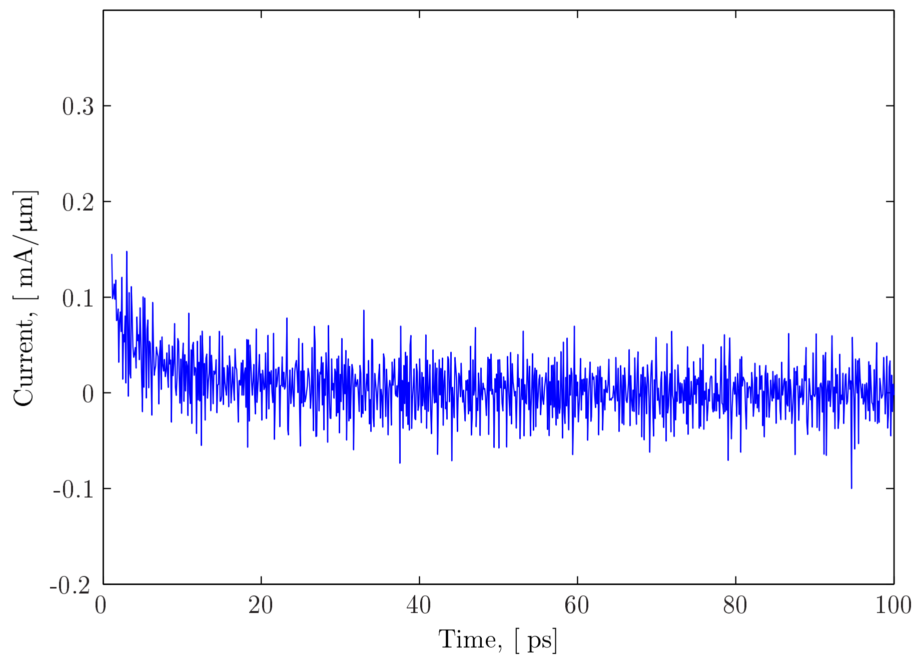

(a) Current through the *pn*-diode during the switching process

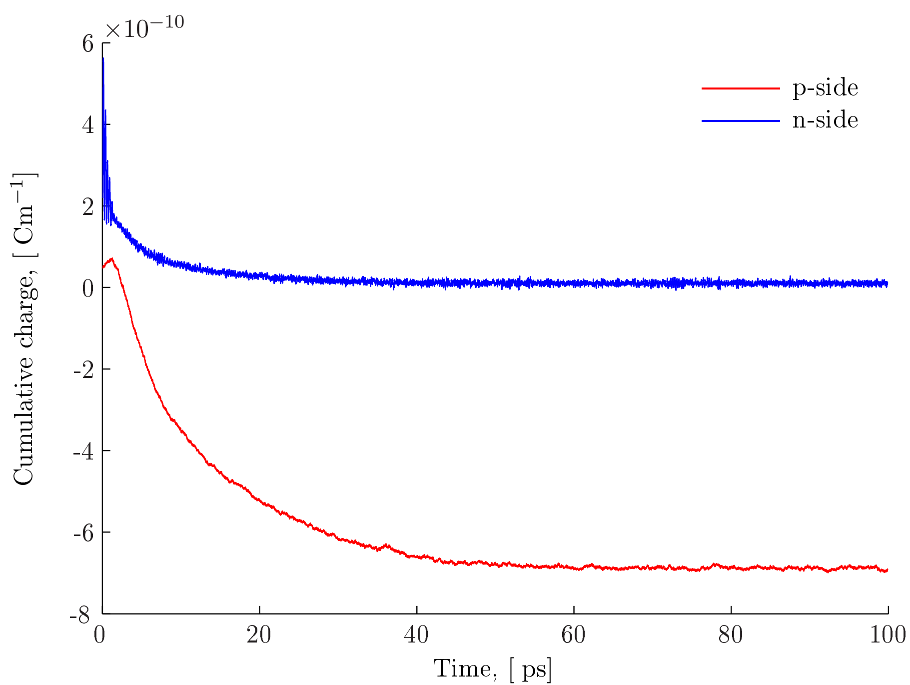

(b) Cumulative charge that has entered the left contact and exited the right contact.

Figure 6.17: Switching of the CMT *pn*-diode from the conducting to the non-conducting state.

Chapter 7

APD model

In this chapter, we will in section 7.1 briefly explain how an APD works before we describe the details of the APD model as we have implemented it in the Monte Carlo simulator. The architecture of our model component is described in section 7.2. The physical process of impact ionisation is sketched in section 7.3 and the model as we have implemented it to the simulator is described in section 7.4. Section 7.5 gives an overview of the model in pseudo code, and the details of the photo excitation models is given in section 7.5.1.

7.1 Principle of operation

An APD is a photodetector, a device which may transform a light signal to a current pulse. An important application of APDs are as photodetectors for LIDARs (Light Detection And Ranging). A LIDAR illuminates a target by laser pulses and detects the back-scatter. Object imaging and mapping by LIDAR has applications in a wide range of fields, ranging from studies of atmospheric composition to geological surveying as well as military applications [44]. Another important application for APDs is the scintillation counter [45]. A scintillator is a crystal which fluoresces when struck by ionising radiation, the light from the crystal may be detected and converted to an electrical signal using an APD.

Different semiconductors are suited as detectors for different parts of the electromagnetic spectrum determined by the quantum efficiency of the material. The definition of quantum efficiency is the fraction of photons of

given wavelength which are converted to electron-hole pairs. $Cd_xHg_{1-x}Te$ has a high quantum efficiency in the interval $3 - 15$ µm depending on the alloy composition. Thus $Cd_xHg_{1-x}Te$ is a detector material covering both of the atmospheric windows in the infrared spectrum. For $x = 0.28$, the material is suited for mid-wave infrared detection, i.e. wavelengths in the range $3 - 5$ µm.

The APD that we will study here is in principle a *pn* junction under reverse bias. A photon which is absorbed in the depletion region may generate carriers by the photoelectric effect. Carrier multiplication is caused by the impact ionisation process described in the following section. These carriers will eventually reach the contacts of the device, resulting in a measurable current gain.

$Cd_xHg_{1-x}Te$ is a highly sensitive detector material which is also low in noise [46]. The low multiplication noise is due to a large asymmetry between the impact ionisation rates of electrons and holes in CMT, this reduces the excess noise which stems from the stochastic nature of the multiplication process. An especially useful property of APDs is that the excess noise is in dependant of the gain. As a consequence, the reverse bias may be increased to increase the signal strength from the APD without increasing the noise at the same time. This makes these devices useful detectors for signals of very low intensity; devices capable of detecting single photons have been reported [47].

7.2 APD architecture

The model APD we will study here is a *pin* device operated under reverse bias. The *i*-region of such a device should be near intrinsic; in practise, it is often weakly doped with donors. The interface between the *p* and *i* region resembles the *pn*-junction studied in the previous chapter, but because of the weak doping, the depletion region extends far into the *i*-region. Under reverse bias there will be a reinforced electric field across the depletion region.

Our model APD is sketched in figure 7.1. The acceptor density is 1×10^{16} cm^{-3} at the *p* side and the donor densities are 5×10^{14} cm^{-3} and 1×10^{17} cm^{-3} respectively for the *i* and *n*+ regions. We believe including a heavy doped contact region at the *p*-side would help increase device performance, and should be considered for future simulations. The same device has been used for the simulations presented in chapter 8. We have kept the doping den-

sities low in order to avoid degeneracy and hence the need for considering the Pauli principle. Table 7.1 gives an overview of the device measures and simulation parameters used with the simulations presented in chapter 8.

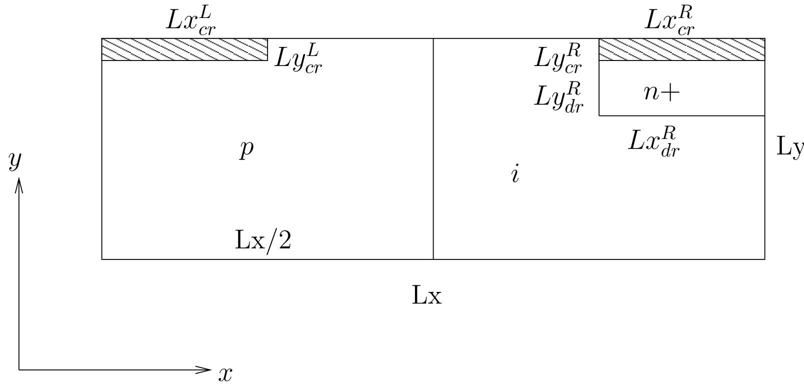

Figure 7.1: The geometry of the APD device. The shaded regions represent the contact regions.

7.3 The Auger and impact ionisation processes

The Auger and the impact ionisation processes are non-radiative recombination and generation processes occurring in semiconductors. The Auger and impact ionisation processes are inverse of each other; the Auger processes are associated with carrier recombination and impact ionisation processes with carrier generation. These processes exists in a few different variants, depending on whether localised states or phonons are involved. Ridley [48] describes five basic Auger processes; here we will focus on the Auger 1 process because it is the dominant process occurring in narrow gap semiconductors. The impact ionisation process implemented in the Monte Carlo simulator is the inverse of the Auger 1 process.

The Auger 1 process is initiated by a collision between two electrons where one of the electrons falls down into the valence band; the energy of the annihilated electron hole pair is absorbed by the other electron.

The inverse impact ionisation process is initiated with a high energetic electron which causes an ionising collision with the lattice, thus generating an electron hole pair. In this process, the initial electron loses energy corresponding to the energy gained by the newly generated electron hole pair.

Lx	3.0 µm
Ly	1.0 µm
$\mathrm{Lx_{dr}}^R$	0.75 µm
$\mathrm{Ly_{dr}}^R$	0.30 µm
$\mathrm{Lx_{cr}}^L = \mathrm{Lx_{cr}}^R$	0.75 µm
$\mathrm{Ly_{cr}}^L = \mathrm{Ly_{cr}}^R$	0.02 µm
Nx	600
h	5 nm
τ	1 fs
τ_f	5 fs
N_A	1×10^{16} cm^{-3}
N_D	5×10^{14} cm^{-3}
N_D^+	1×10^{17} cm^{-3}
T	300 K / 77 K
x	0.28

Table 7.1: Simulation parameters for the APD diode. The symbols are explained in figure 7.1.

The two electrons of the final state are swept to the n-side and the hole to the p-side. Figure 7.2 illustrates the process.

Carriers in the high electric field of the reverse biased pn-junction of an APD are accelerated to high energies, thus impact ionisation becomes an important scattering mechanism in this region of the device. One photo generated electron hole pair in this region may initiate a sequence of impact ionisation, resulting in carrier or avalanche multiplication. If enough carriers are generated, a current gain is measurable at the contacts of the device.

7.4 The impact ionisation model

This section describes the impact ionisation model implemented in our Monte Carlo simulator. We assume that only electrons may initiate impact ionisation events; this is a reasonable assumption for CMT due to the large asymmetry between the impact ionisation rates of electron and holes.

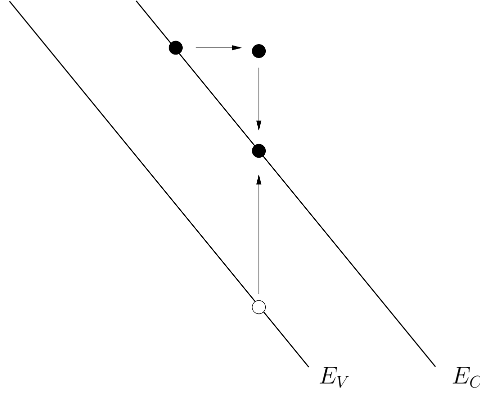

Figure 7.2: Illustration of carrier generation by the impact ionisation process. A high energy electron loses energy to produce an electron hole pair. The figure is from [49].

7.4.1 Scattering rate

The impact ionisation process is modelled as a scattering mechanism following the approach of [50]. Thus, we first need to obtain the scattering rate for the impact ionisation scattering mechanism. Several choices exist, many authors uses the Keldysh formula [50, 51], but we have decided to use the rate obtained by Ridley [48] in order to avoid the use of fitting parameters. The calculation of this rate is described in great detail; the Fermi Golden Rule is used with the matrix element of screened Coloumb interaction. The final expression is:

$$W_{ii} = 4.139 \times 10^{16} \left[\frac{4\sqrt{m_e^* m_h^*}}{m_0} \left(\frac{m_e^*}{m_0} + \mu \right) \left(\frac{1}{\varepsilon_r} \right)^2 \left[\frac{E_i}{E_g} - (1+\mu) \right] \right].$$

In this expression, m_e^* and m_h^* are the effective masses of the conduction and valence band, m_0 the free electron mass, E_i the energy of the electron which initiated the process and $\mu = m_e^*/m_h^*$. The scattering rate reflects that the energy of the incident electron must be higher than the threshold energy

$$E_{th} = \frac{1+2\mu}{1+\mu}$$

to be able to cause impact ionisation. The scattering rate is plotted in figure 7.3.

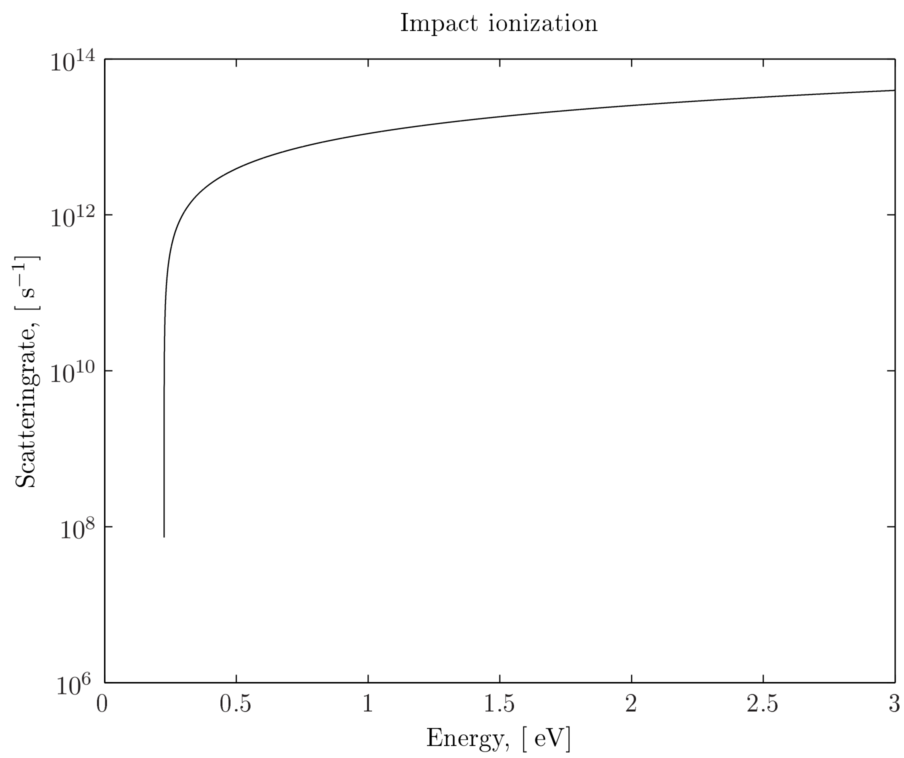

Figure 7.3: The scattering rate for impact ionisation at 300 K used in the Monte Carlo simulator.

7.4.2 Determining the energy loss

The next problem is to find the energy loss, ΔE_i, of the electron that initiated the ionising collision. According to Kinch [52], the total probability of impact ionisation is proportional to the integral

$$P\left(E_i\right) \propto \int_1^{\frac{E_i}{E_g}} \mathrm{d}x \left[\frac{\sqrt{2\left(\left(\frac{E_i}{E_g} - x\right) + 1\right)^2 - 1}\left(2\left(\frac{E_i}{E_g} - x\right) + 1\right)\left(2x - 1\right)\sqrt{\left(2x-1\right)^2 - 1}}{x^4}, \right]$$

where, $x = \Delta E_i/E_g$. From this integral, we have extracted a probability distribution for the energy loss of the electron causing the ionising collision depending on its initial energy. The integral runs over all possible energy losses, thus for a given E_i, the integrand is proportional to the probability distribution for the energy loss. A plot of this integrand for a few different values of E_i is given in figure 7.4, the graphs have been normalised with their maximum values to ease comparison. For energies larger than a few E_g, the shape of the distribution function, including the position of the maximum, shows small changes; we have therefore chosen the three curves in figure 7.4 as approximate distributions to save computations. Once the probability distribution for ΔE_i is known, we sample from it using the acceptance-rejection method described in [27].

7.4.3 Generation of the new electron-hole pair

Once the energy loss of the electron initiating the impact ionisation process is determined, it remains to determine the states of the three carriers after the scattering. The energy of the original electron after the scattering is $E_i - \Delta E_i$, while the loss is divided equally between the generated electron and the hole. In our model, the new electron is created in the Γ-valley while the new hole is created in the heavy hole band. The modulus of the momentum vectors are found using the band structure while the directions of the momenta of all three particles are randomised, adopting the procedure of [51].

Our model takes into consideration the conservation of energy, but not conservation of momentum. The randomisation of the final state momenta is a crude approximation which violates an important fundamental law of

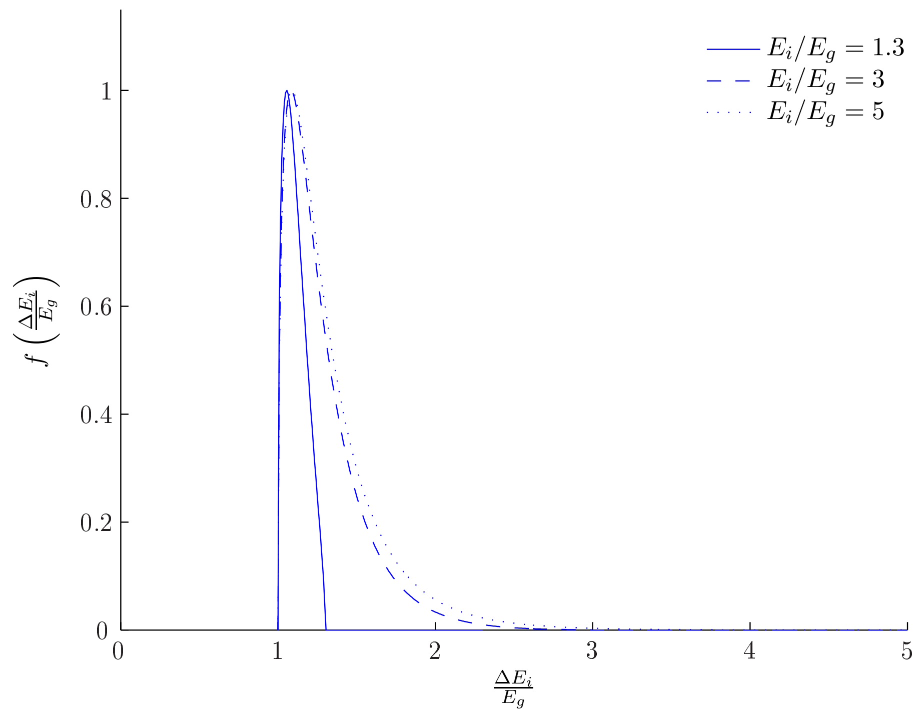

Figure 7.4: Given the energy, E_i of an incident electron in an impact ionisation process, $f(\Delta E_i/E_g)$ is proportional to the probability distribution for the energy loss of the electron during the process.

physics, namely the conservation of momentum. If the number of impact ionisation events taking place during a simulation is large, the randomisation will ensure that there is no bias towards any side; and thus, considering the total of all the impact ionisation events, one can imagine that the momentum on average is near conserved.

An overview of the implementation of the scattering mechanism is given in pseudo code below:

```
< Determine energy loss:
     - choose distribution function
     - sample from chosen distribution function
       using accept-reject method >

FinalEnergy = InitialEnergy - EnergyLoss
k = k(FinalEnergy)
< randomize direction of momentum >

< Generate electron-hole pair:
     k = k(deltaEi/2)
     position = position of initial electron
     < randomize directions of momenta >
     valley = Gamma
     band =  heavy hole >
```

7.5 Overview of program implementation

Simulation of the APD simulation is conducted in two parts; first, the *pin*-structure is simulated under reverse bias until the stationary Monte Carlo equilibrium is reached. In this part of the simulation, Poisson's equation is solved every field adjusting time step. We have used approximately 50 000 superparticles of each species and the Dirichlet boundary conditions $V_L = -3.0$ V and $V_R = 0.0$ V to obtain the carrier distribution shown in figure 7.6. The figure shows that most of the particles participating in the simulation are located in the near charge neutral areas where impact ionisation has a low probability of occurring.

To increase the efficiency of the simulation, this carrier distribution along with with the corresponding electric field will be frozen in the second part of the simulation. One electron-hole pair is optically generated, and in addition

to this pair, we track in time only the carriers generated by the impact ionisation process. The carriers are considered electrons and holes carrying the elementary charge. They participate in free flights and scatterings, but we assume their contribution to the electric field within the device is negligible. The injection of superparticles at the contacts is stopped, but the simulated carriers are allowed to leave the device through the contacts. The current measured at the contacts represents the current gain. This implies that if any dark current would be running through the diode during the simulation, it would have been artificially set to zero.

```
< Perform simulation to obtain (or read) electric field >

for each simulation

   < Generate electron hole pair due to photo-excitation >

   for all timesteps

      for all electrons
         < flight >
         < scatter, including impact ionization mechanism>
      end

      for all holes
         < flight >
         < scatter >
      end

      < Absorb particles at contacts >
      < Measure current at the contacts >
      < Collect statistics >

   end

   < Collect statistics >

end
```

Figure 7.5: Overview of the program implementation of the APD model.

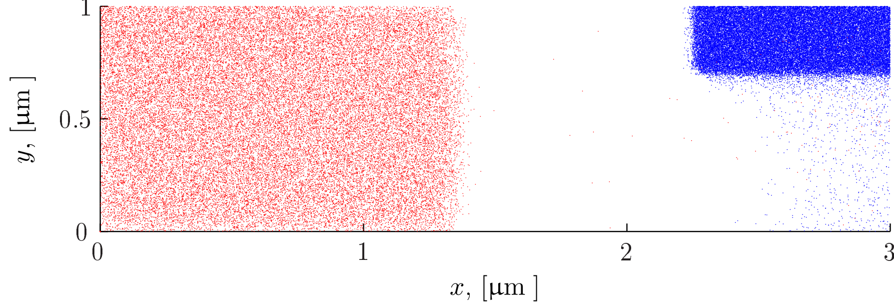

Figure 7.6: Spatial distribution of electron (blue) and hole (red) positions in the reverse biased *pin*-structure.

7.5.1 Photo excitation

The initial electron hole pair starting the avalanche process in an APD photodiode is generated by a photon with energy E_γ impinging on the i-region of the diode. The photon energy needs to be larger than the band gap to be able to ionise an atom; the remaining energy will be split among the electron and hole. The photon energy can thus be written

$$E_\gamma = E_g + E_h + E_e. \tag{7.1}$$

For the simulations presented in the next chapter, a 4.0 μm photon has been used to initiate the avalanche process. The generated particles are assumed to be a heavy hole and an electron in the Γ valley. The resulting electron energy, E_e and hole energy, E_h, is found using the band structure. Figure 7.7 shows equation 7.1 plotted as a function of $k = |\mathbf{k}|$. The electron-hole pair is given the k found at the intersection of the two curves while the direction chosen at random. The hole is given the negative of the electron $\mathbf{k}$-vector to preserve the momentum in the ionisation process. The position of the initial electron hole pair is fixed to the depletion region of the i-region of the *pin*-structure.

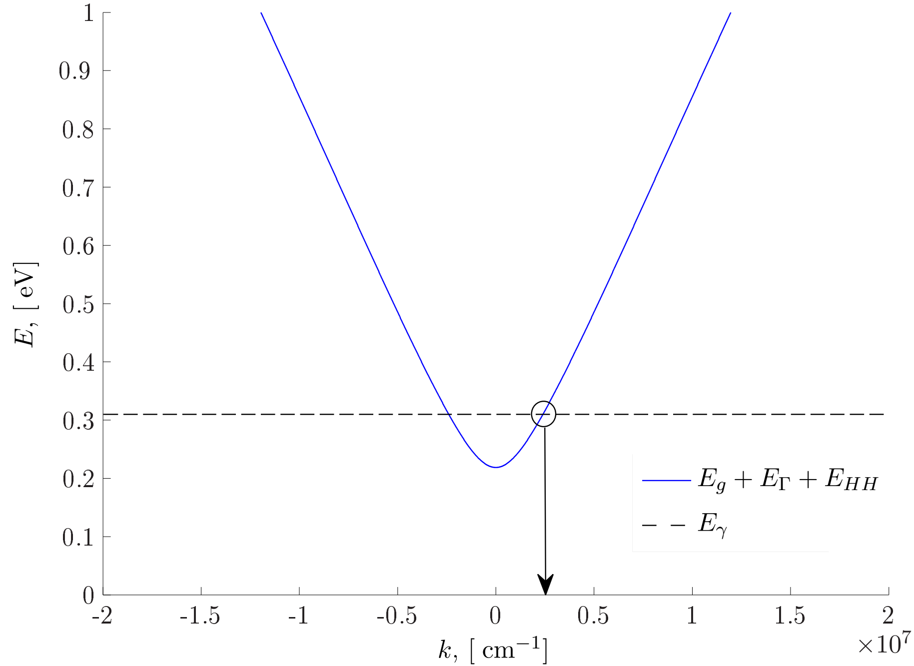

Figure 7.7: Finding the modulus of the **k**-vector from the band structure.

```
< Determine photon energy from wavelength>

< Assign fixed position in i-region >

< determine electron |k| from band structure >
< randomize direction of momentum >
< Transform electron k-vector to cartesian coordinates >
< valley  = Gamma >

< Assign hole k-vector using conservation of momentum >
< band = heavy hole >
```

Figure 7.8: Pseudo code giving an overview of the photo-generation of an electron-hole pair.

Chapter 8

APD simulation results

In this chapter the simulation results for the reverse biased $Cd_{0.28}Hg_{0.72}Te$ APD of figure 7.1 will be presented. We have studied the current gain in terms of the carrier multiplication in the device under different conditions, including variation in the photon energy and lattice temperature. First, we will have a peek at the behaviour of the carriers inside device during the multiplication process.

8.1 Distribution of carriers inside the device

In figure 8.1, we have extracted the carrier positions within the device at a few selected time steps during the simulation. The simulation was allowed to run until we could observe that all the carriers had exited the device, approximately a few hundred picoseconds. The top left plot shows the initial photogenerated electron hole pair, it is accelerated in the electric field for a few hundred femtoseconds before the the first impact ionisation process occurs. The electrons, which have small effective masses compared to the holes, drift faster towards the contact at the n-side than the holes towards the p-side. As the impact ionisation events continue to happen, more and more holes appear near the n-side of the component. As the electrons reach the n contact, they exit the simulation. In a real device which obeys charge continuity, the electrons would not be allowed to escape the device while the holes are still on their way to the contact. They would have to wait for the holes to reach the opposite contact and then recombination would take place. In our simulations, depending on the bias voltage, the holes either succeed at

exiting the component or they accumulate at the p-side of the device, which is a sign of poor performance of this particular component. This effect might either be due to unphysical large fluctuations in the electric field due to the large superparticle charge, or it might be due to poor architecture design. In the latter case, including a $p+$ region close to the p-contact would give rise to an electric field which could pull the holes faster towards the contact.

As the electrons move out of the high electric field, they lose energy and the probability of impact ionisation events decreases. Consequently, new electron hole pairs are generated at a lower rate and eventually the generation process dies out. One light pulse may thus be associated with one current pulse.

8.2 Switching time

The switching time for the APD diode has been measured when switching from forward bias voltage corresponding to Dirichlet boundary conditions $V_L = V_R = 0.0$ V to reverse bias corresponding to Dirichlet boundary conditions $V_L = 0.0$ V and $V_L = -8.0$ V. Figure 8.2 shows the current dropping off during the transition. The figure indicates a switching time just above ~ 500 ps.

8.3 Multiplication and noise

The multiplication factor is the total number of electron hole pairs generated from the initial photogenerated pair of carriers. We have measured the average multiplication factor and its standard deviation for two different lattice temperatures and two different photon wavelengths. The multiplication factor is a measure of the current gain and hence the performance of the APD, while the standard deviation is related to the noise.

The simulation results presented in table 8.1 are averages over 5000 simulations performed at a reverse bias of -3.0 V, meaning that the Dirichlet boundary conditions to the Poisson solver was set to -3.0 V at the p-side and 0.0 V at the n-side.

According to table 8.1, the multiplication is slightly larger for both wavelengths when the device is cooled. The impact ionisation rate is slightly larger at 300 K than 77 K, but the difference is believed to be too small, a

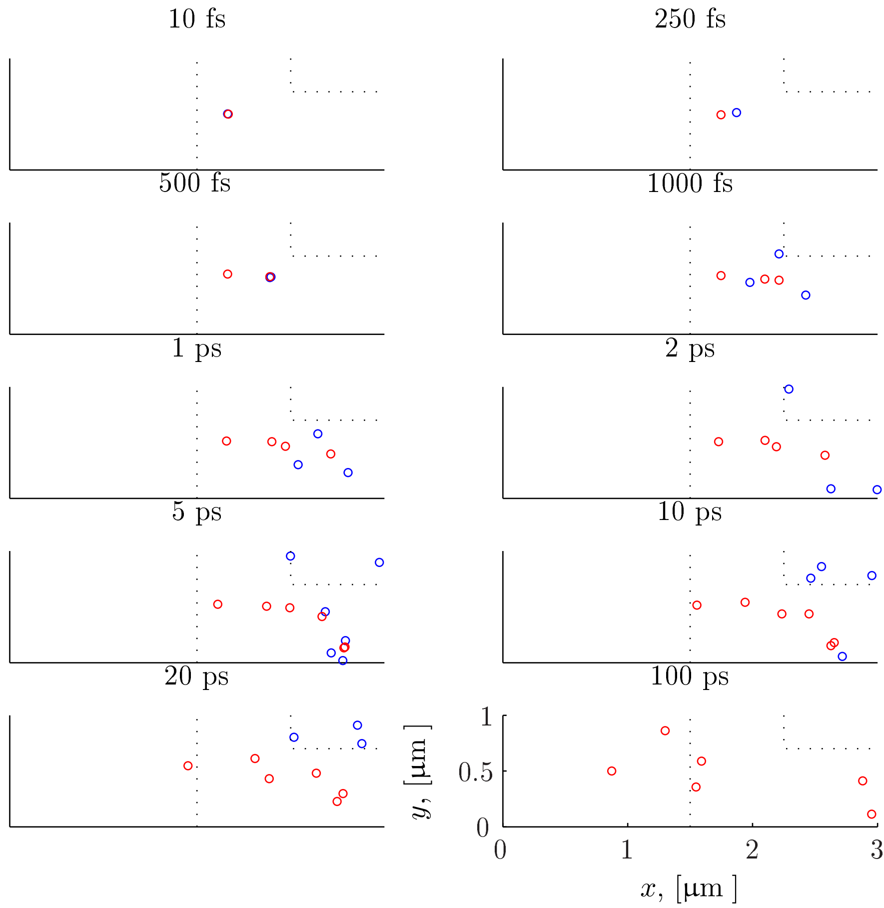

Figure 8.1: Carrier positions at selected time steps during the simulation. This simulation was carried out at a reverse bias of 3.0 V.

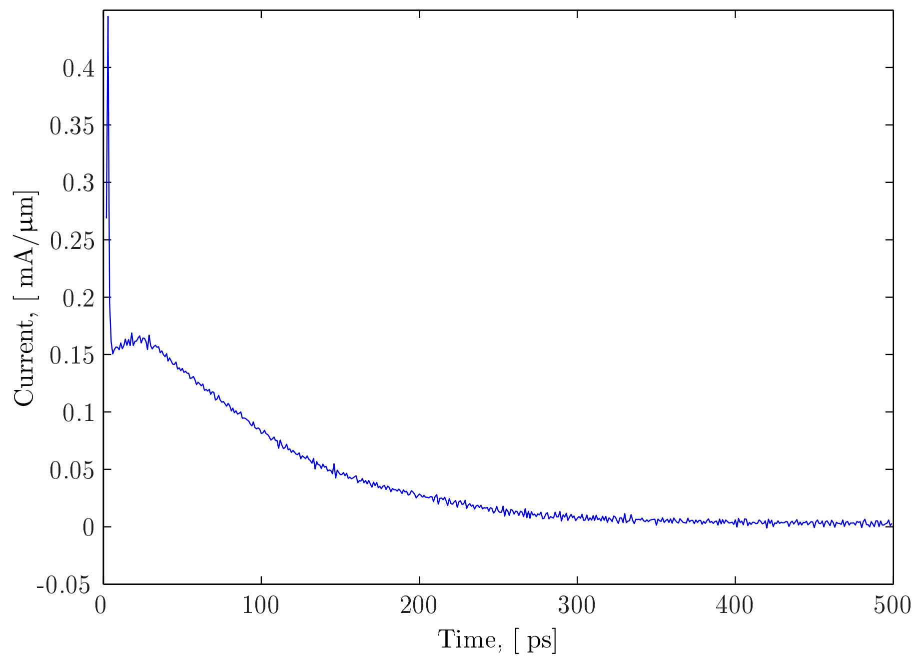

(a) Current through the APD during the switching process

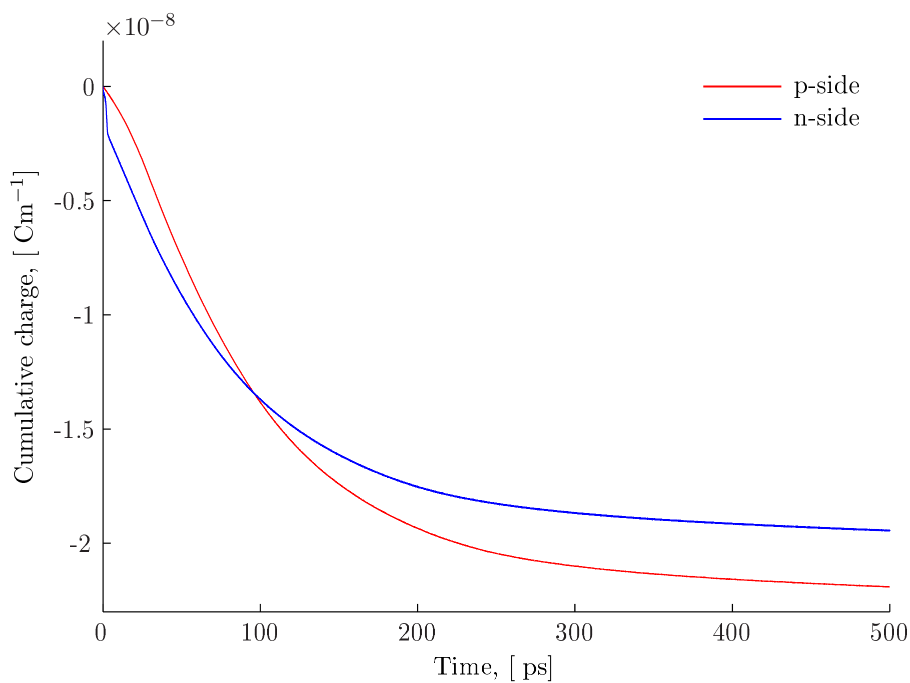

(b) Cumulative charge that has entered the left contact and exited the right contact.

Figure 8.2: Switching of the CMT APD from the conducting to the non-conducting state.

factor of the order ~ 1.1, to be directly responsible for the deviation. However the other scattering rates, as e.g. the polar optical scattering rate is considerably higher at room temperature. When scatterings occur more often, the electron mobility is reduced. Thus the carriers in the cooled device reach higher velocities, which, combined with a lower threshold energy for impact ionisation, agrees with a larger multiplication factor.

The excess noise factor, F, is estimated using the formula [50]:

$$F(M) = 1 + \frac{\sigma_M}{M}^2,$$

where M is the mean multiplication gain and σ_M the standard deviation. For our simulations, the excess noise is indeed independent of gain, and the values, just above 1, agrees with what has been observed in previous studies [50].

	Photon wavelength	M	σ_M	Excess noise
$T = 300$ K	3.0 µm	12.8	6.6	1.27
	4.0 µm	10.3	5.3	1.26
$T = 77$ K	3.0 µm	16.5	7.7	1.22
	4.0 µm	13.3	6.2	1.22

Table 8.1: Multiplication, M, and standard deviation, σ_M obtained at a reverse bias of -3.0 V. The results are averaged over 5000 simulations.

8.4 Current impulse response

The bandwidth of the device is related to the time it takes from a photon hits the detector until the corresponding current pulse has faded out. The bandwidth is of great interest for APDs to be used as the photodetecting components of LIDARs, but as far as we know, little research has been done on the current response CMT diodes so far.

In figure 8.3, the number of carriers exiting at one of the contacts per femtosecond is plotted as a function of time for a simulation performed at a reverse bias of 7.0 V. The generating photon had a wavelength 4.0 µm.

The plot shows that the bandwidth for this component is limited by the holes. At 8 ns, all the holes has exited the device. The logarithmic x-axis of the plot obscures the fact that most of the holes exit the simulation during

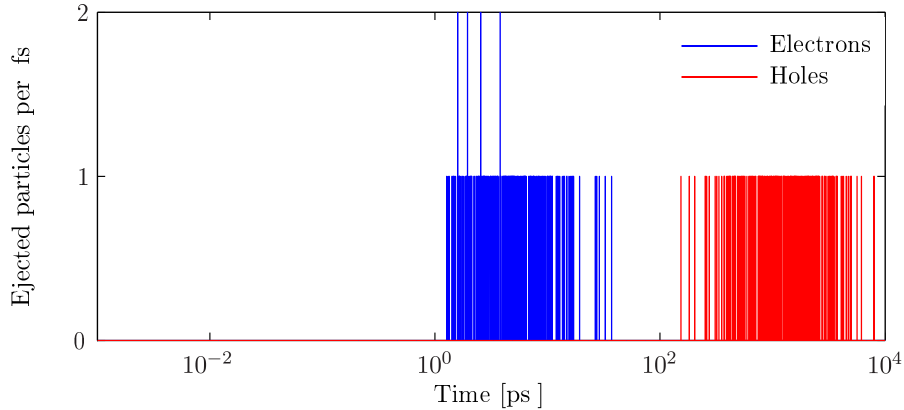

Figure 8.3: Reverse bias voltage: −7 V,photon wavelength 4.0 μm

the time interval between 300 ps and 2 ns, followed by a tail which is close to reaching zero at 5 ns.

It should be noted that the circuit surrounding the APD is not part of our Monte Carlo model. As a consequence, there is no charge continuity condition imposed on the contacts in our model, and thus there is reason to believe that the time the model predicts it would take to exit the holes from the device may be too long.

8.5 Gain-voltage characteristics

Figure 8.4 shows the multiplication-voltage characteristics of the simulated diode. As observed in other studies, e.g. Derelle *et al.* [51], the gain curve is exponential. This is a property of HgCdTe APDs related to the high asymmetry of the impact ionisation coefficients of electron and holes.

Derelle *et al.* has studied the multiplication gain under variations in which scattering processes are included in the model [51]. The authors conclude that alloy scattering has a large effect on the multiplication and excess noise factor; they observe a steeper multiplication voltage characteristics for the simulations which include the alloy scattering mechanism. The alloy scattering is assumed to be completely random and isotropic in this model. In our model the potential for the alloy scattering is not set for the simulations presented here, thus alloy scattering does not happen in our simulations.

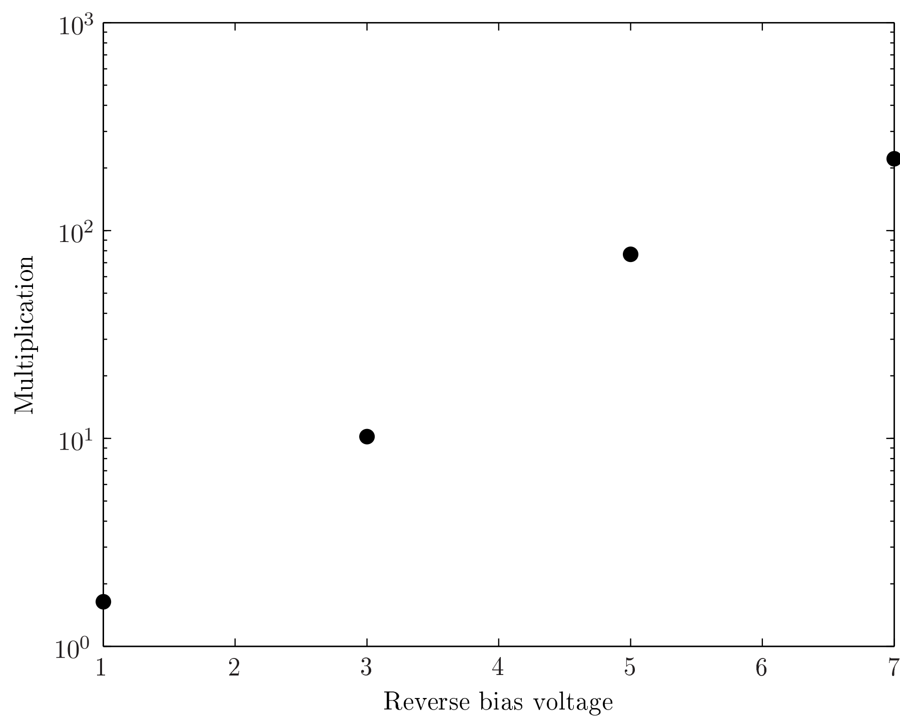

Figure 8.4: T=300K, photon wavelength 4.0 μm.

Chapter 9

Discussion and further work

At the moment, several research groups work on Monte Carlo simulation of APD-diodes. On the contrary, only few MC studies exist of the simple *pn*-diode, and these are mainly from the 1980s.

The recent APD studies focus mainly on modelling and simulating gain and noise in existing components in order to study device performance. Our focus has been on the Monte Carlo method itself; to establish the difficulties of using the Monte Carlo method. Our model is not tuned to experimental results and contains no fitting parameters. Our model devices are chosen for simplicity rather than for high performance. Our focus has been to shed some light on general problems which arise when using the Monte Carlo technique for studying devices based on *pn*-junctions.

The research on APD structures conducted up until recent operate in the low photocurrent limit [53, 46, 50]; it is assumed that the charge of the optically generated cloud of electron hole pairs is small enough that the electric repulsion between them can be neglected in comparison to the large applied bias. This assumption implies that the electric field is calculated only at the beginning of the simulation and stays frozen throughout. It is only since spring 2011 that simple Fermi-Poisson solvers [53, 50] has been replaced by self-consistent solution of the Monte Carlo model and Poisson's equation [46, 54]. The low photocurrent assumption was relaxed first by Bertazzi *et al.* in 2011 [54], but it still remains to do this for CMT APDs. Our model is in principle prepared for doing this at this stage.

The APDs current response to a light pulse in CMT APDs has been studied

using the Monte Carlo model [54] and a 1D deterministic model based on carrier generation [55]. The latter study explains that the response time is due to the large capacitive effect of the metal contacts. The former explains the response time in terms of the gain. A longer tail of the current response curve is observed for larger gains; the increased number of offspring carriers need more time to leave the device. Our model is in agreement with both of these models, but in addition, it points at the importance of the large difference in electron and hole velocities. Based on our simulation results, we suggest to explore the possibility of coupling the Monte Carlo method with the solution of Maxwell's equations to study the significance of the displacement current on the current response time.

Further development of the Monte Carlo simulator includes development of the Poisson solver. A cylindrical 2D solver will prepare the simulator for modelling a new class of devices, as will the inclusion of a 3D solver. The 2D solver currently included in the simulator consumes about 50% of the simulation time, solving the 3D problem strengthens the need for a fast solver. This can be achieved within the framework of the successive over relaxation method by applying multigrid techniques. Another alternative which may be considered is the Fast Multipole Method (FMM) [5]. This method relies on reducing the complexity the many-body problem before solving it, thus reducing the solution time.

9.1 Further work

During the work with this thesis, we have identified a number of details that will improve the Monte Carlo simulator:

- Include the full band structure information and provide interoperability with ab-initio electronic structure codes such as Wien2k.
- The impact ionisation model should be improved by taking into account conservation of momentum in addition to energy conservation.
- The ohmic contact model should be fitted for the CMT material. It is necessary to implement the Ramo-Shockley particle boundary conditions. Furthermore, detailed simulation of the contact region using the charge enhancement method should be considered.

In the discussion section, a few topics relevant for ongoing research in the field of APDs were mentioned. In addition, we suggest:

- Use the model to solve Poisson's equation self-consistently during APD simulation in order to study larger photocurrents or THz switches.
- The iterative Poisson solver which has been developed can be combined with the multigrid technique prior to parallellisation.

Chapter 10

Conclusions

The Monte Carlo simulator which has been developed as a student project at FFI has during this work been made capable of modelling devices. A fast Poisson solver which relies on the successive overrelaxation method has been implemented and an impact ionisation model has been implemented in order to make the simulator capable of modelling APDs.

During this work, two simple *pn*-junction devices has been simulated, a *pn*-diode and an APD. The device characteristics, including current-voltage characteristics and switching times have been obtained. Our simulation results of the *pn*-diode has shown that there may be a small formation of electron plasma at the *p*-side of a CMT *pn*-diodes. For the APD, we have studied multiplication and noise and obtained the gain-voltage characteristics.

We simulated simple devices in order to discuss a few problematic aspects of the Monte Carlo method which arise when simulating CMT *pn*-junctions. Within the framework of the Monte Carlo method, the dark current needs to be neglected for CMT APDs. We have pointed to the fact that the current-impulse response may turn out inaccurate due to violation of the continuity equation in the surrounding circuit. Furthermore, we believe that the self-consistent solution of the transport equations and Poisson's equation using the Monte Carlo method is well suited for studying large photocurrents in APDs because the frozen field assumption is easily relaxed within the Monte Carlo framework.

Appendix A

Energybands and effective masses

The energy bands and scattering rates are corner stones of the Monte Carlo model. They have not been altered during the work with this thesis, thus they are presented here in the appendix. More details are presented in the theses of Norum [8], Olsen [9] and Skåring [10].

The electron band band structure used in the Monte Carlo simulator is the analytical and isotropic approximation

$$\gamma(k) = E(1 + \alpha E) = \frac{\hbar^2 k^2}{2m^*}, \tag{A.1}$$

where $\alpha = (1 - m_\Gamma^*/m_e)^2/E_g$ and E_g is the band gap at the Γ point. Here, m^* are the effective masses of the three valleys included in our model, Γ, L and X.

The effective mass of the Γ valley at the bottom of the conduction band is in our model $m_\Gamma^* = \frac{3\hbar^2 Eg}{(16.56 \times 10^{-10} eC)^2}$, thus depends on the alloy fraction and temperature via the band gap dependancy. The effective masses of the L and X valleys are $m_L^* = 0.222 m_e$ and $m_X^* = 0.580 m_e$ where m_e is the free elctron mass. These valleys are high in energy, 1.5 eV and 2.5 eV respectively, and therefore rarely active in $Cd_xHg_{1-x}Te$.

The current heavy hole the light hole band models are described in Skåring's master's thesis [10]. The bands are reproduced together with the electron band structure of the Γ valley in figure A.1. The hole bands are isotropic

with continous derivatives. The effective hole masses are $m^*_{HH} = 0.530 m_e$ and $m^*_{LH} = m^*_{\Gamma}$.

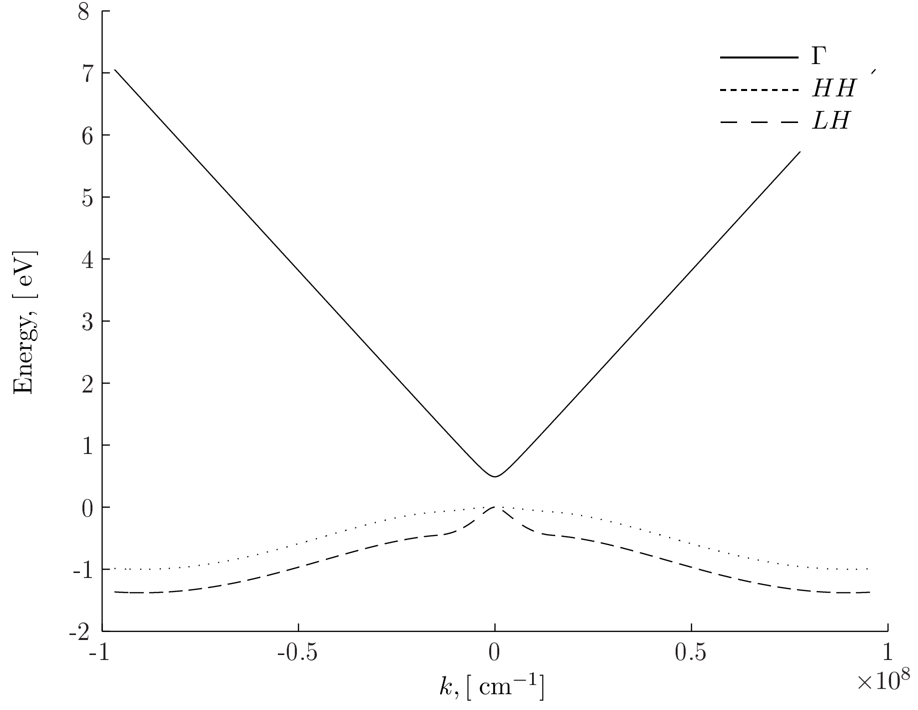

Figure A.1: The band structure of the Γ valley, the heavy (HH) and light (LH) hole band at 300 K.

Appendix B

Scattering rates

The intravalley and intraband scattering rates included in our Monte Carlo model as functions of the Γ valley and heavy hole band energy are presented in figures B.1 and B.2 respectively. In addition, intervalley and interband scattering rates are included in the model.

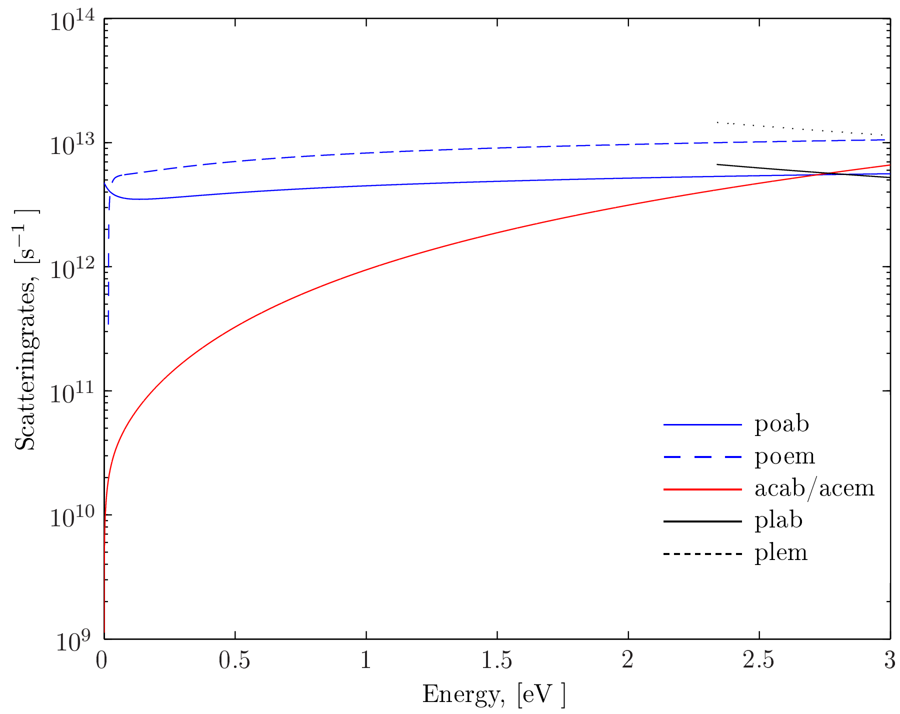

Figure B.1: The scattering rates for the Γ valley at 300 K. Poab/poem means polar optical absorption/emission, acab/acem corresponds to acoustic phonon scattering and plab/plem to plasmon scattering.

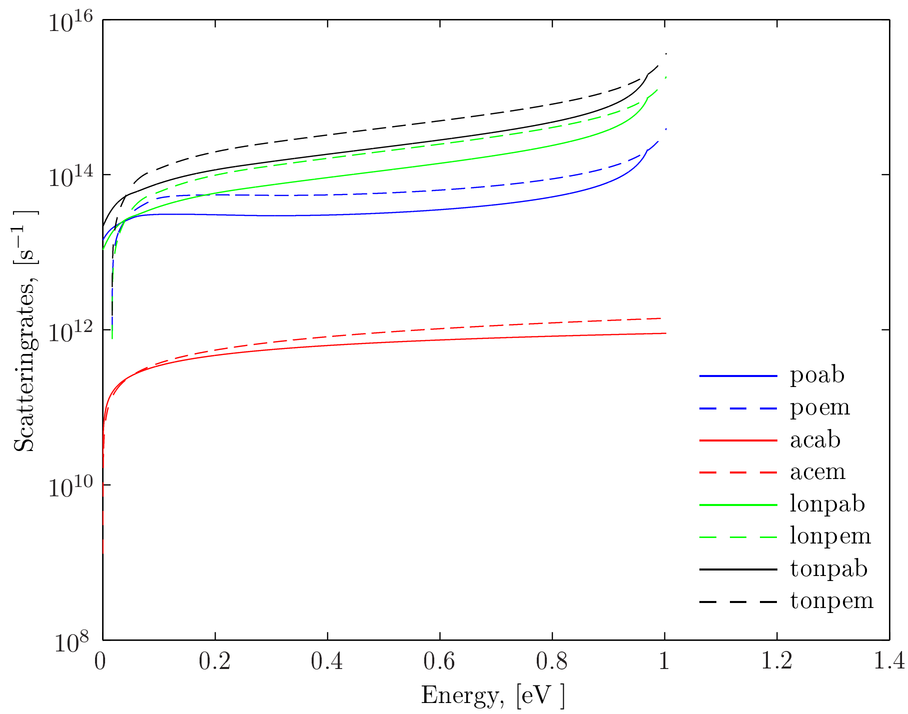

Figure B.2: The heavy hole scattering rates at 300 K. Poab/poem means polar optical phonon absorption/emission, acab/acem corresponds to acoustic phonon scattering, lonpacab/lonpacem and tonpacab/tonpacem to longitudinal and transversal nonpolar optical phonon scattering respectively.

Bibliography

[1] J. P Laurenti, J. Camassel, A. Bouhemadou, B. Toulouse, R. Legros, and A. Lusson. Temperature dependence of the fundamental absorption edge of mercury cadmium telluride. *Journal of Applied Physics*, 67(10), 1990. http://dx.doi.org/10.1063/1.345119.

[2] M. Cardona and P. Yu. *Fundamentals of Semiconductors : Physics and Materials Properties*. Springer, 2010.

[3] S. Raimes. *Many-Electron Theory*. North-Holland Publishing Company, 1972.

[4] http://en.wikipedia.org/wiki/File:Fcc_brillouin.png. Visited 06.01.2011.

[5] D. Vasileska, S. M. Goodnick, and G. Klimeck. *Computational Electronics - Semiclassical and Quantum Device Modelling and Simulation*. CRC Press, 2010.

[6] J. Singh. *Electronic and Optoelectronic Properties of Semiconductor Structures*. Cambridge, 2003.

[7] C. Jacoboni and P. Lugli. *The Monte Carlo Method for Semiconductor Device Simulation*. Wien: Springer, 1989.

[8] O. C. Norum. Monte Carlo simulation of semiconductors - program structure and physical phenomena. Master's thesis, Norwegian University of Science and Technology, Department of Physics, 2009.

[9] Ø. Olsen. Construction of a transport kernel for an ensemble Monte Carlo simulator. Master's thesis, Norwegian University of Science and Technology, Department of Physics, 2009.

[10] Ø. Skåring. Ultrashort relaxation dynamics in laser excited semiconductors. Master's thesis, Norwegian University of Science and Technology, Department of Physics, June 2010.

[11] T Brudevoll, A. K. Storebø, Ø. Skåring, O. C. Norum, Ø. Olsen, C. Kirkemo, and M. Breivik. Time-resolved laser spectroscopy of semiconductors - physical processes and methods of analysis. In A. V. Andreev, editor, *Femtosecond-Scale Optics*. INTECH, 2011. ISBN 978-953-308-56-9.

[12] A. K. Storebø, T. Brudevoll, Ø. Skåring, C. N. Kirkemo, O. C. Norum, and Ø. Olsen. Cooling dynamics of photo-excited carriers in HgCdTe. To be published in J. Phys.: Conference Series, (2011).

[13] T. Brudevoll. *Monte Carlo Algorithms for Simulation of Hole Transport in Homogenous Semiconductors*. PhD thesis, Norges Tekniske Høyskole, 1991.

[14] D. S. Kim. *Monte Carlo Modeling of Carrier Dynamics in Photoconductive Terahertz Sources*. PhD thesis, Georgia Institute of Technology, 2006.

[15] A. Abramo, F. Venturi, E. Sangiorgi, Higman J., and B. Ricco. A numerical method to compute isotropic band models from anisotropic semiconductor band structures. *IEEE Transactions on Computer-Aided Design of Integrated Circuits ans Systems*, 12(9), 1993. http://dx.doi.org/10.1109/43.240080.

[16] B. Lund. *Monte Carlo Simulation of Charge Transport in Semiconductors and Semiconductor Devices*. PhD thesis, Norwegian Institute of Technology, March 1992.

[17] R. W. Hockney and J. W. Eastwood. *Computer Simulations Using Particles*. McGraw Hill Inc., 1981.

[18] C. Moglestue. *Monte Carlo Simulation of Semiconductor Devices*. Chapman & Hall, 1993.

[19] K. Hess, editor. *Monte Carlo Device Simulation: Full Band and Beyond*. Kluwer Academic Publishers, 1991.

[20] T. Gonzales and D. Pardo. Physical models of ohmic contacts for Monte Carlo device simulation. *Solid-State Electronics*, 39(4), 1996. http://dx.doi.org/10.1016/0038-1101(95)00188-3.

[21] G. U. Jensen. *Monte Carlo Simulation of III-V Semiconductor Devices.* PhD thesis, Norwegian Institute of Technology, June 1989.

[22] R. J. Mills, G. M. Dunn, M. B. Walker, A. B. Daniels, P. J. Bishop, K. O. Jensen, and B. K. Ridley. Monte Carlo simulation of wide AlGaAs barriers. In *Proceedings of IEEE/Cornell Conference on Advanced Concepts in High Speed Semiconductor Devices and Circuits*, 1993. http://dx.doi.org/10.1109/CORNEL.1993.303119.

[23] P. D. Yoder, K. Gartner, and W. Fichtner. A generalized Ramo-Shockley theorem for classical to quantum transport at arbitrary frequencies. *Journal of Applied Physics*, 79(4), 1996. http://dx.doi.org/10.1063/1.361074,.

[24] V. Srivastav, R. Pal, B. L. Sharma, V. Mittal, V. Gopal, and H. P. Vyas. Electrical properties of titanium-HgCdTe contacts. *Journal of Electronic Materials*, 34(3), 2005. http://dx.doi.org/10.1007/s11664-005-0208-0.

[25] V. Gruzinski, S. Kersulis, and A. Reklaitis. An efficient Monte Carlo particle technique for two-dimensional transistor modelling. *Semiconductor Science and Technology*, 6(7), 1991. http://dx.doi.org/10.1088/0268-1242/6/7/006.

[26] A. Tveito and R. Winther. *Introduction to Partial Differential Equations: A computational Approach.* Springer, 2005.

[27] M. Hjorth-Jensen. Lecture notes on computational physics. http://www.uio.no/studier/emner/matnat/fys/FYS3150/h08/undervisningsmateriale/LectureNotes/lecture2008.pdf, 2008. Univeristy of Oslo.

[28] W. F. Ames. *Numerical Methods for Partial Differential Equations.* Academic Press, 3 edition, 1992.

[29] M. Saranti, J. Tang, S. M. Goodnick, and S. J. Wigger. Numerical challenges in particle-based approaches for the simulation of semiconductor devices. *Mathematics and Computers in Simulation*, 62(3-6), 2003. http://dx.doi.org/10.1016/S0378-4754(02)00229-X.

[30] W. H. Press, S. A. Teukolsky, W. T. Vetterling, and B. P. Flannery. *Numerical Recipes in Fortran 77: The Art of Scientific Computing.* Cambridge Univeristy Press, 2 edition, 1992.

[31] D. R. Kincaid and E. W. Cheney. *Numerical Analysis: Mathematics of Scientific Computing*. Brooks/Gole Publishing Company, 1996.

[32] J. E. Flaherty. Course notes - partial differential equations. www.cs.rpi.edu/~flaherje/pdf/pde9.pdf. Visited 25.02.2011.

[33] D. Vasileska, D. Mamaluy, H. R. Khan, K. Raleva, and S. M. Goodnick. Semiconductor device modeling. *Journal of Computational and Theoretical Nanoscience*, 5(1-32), 2008. http://dx.doi.org/10.1166/jctn.2008.002.

[34] http://en.wikipedia.org/wiki/Debye_length. Visited 16.05.2011.

[35] P. W. Rambo and J. Denavit. Time stability of Monte Carlo device simulation. *IEEE Transactions on Computer-Aided Design of Integrated Circuits and Systems*, 12(11), 1993. http://dx.doi.org/10.1109/43.248084.

[36] S. M. Sze. *Semiconductor Devices, Physics and Technology*. Wiley, 2 edition, 2001.

[37] P. Capper, editor. *Properties of Narrow Gap Cadmium-bases compounds*. Institution of Engineering and Technology, 1994.

[38] R. W. Miles. Electron and hole mobilities in HgCdTe. In P. Capper, editor, *Properties of Narrow Gap Cadmium-based compounds*. Institution of Engineering and Technology, 1994.

[39] C. Moglestue. Monte Carlo particle simulation of the hole-electron plasma formed in a p-n junction. *Electronics Letters*, 22(7), 1986. http://dx.doi.org/10.1049/el:19860270.

[40] K.A. Ingebrigtsen and A. Tonning. Forelesninger i fysikalsk elektronikk. Seksjon for fysikalsk elektronikk, NTH, 1979.

[41] P. Würfel. *Physics of Solar Cells, From Principles to New Concepts*. Wiley-VCH, 2005.

[42] K Jozwikowski, J. Piotrowski, W. Gawron, A. Rogalski, A. Piotrowski, J. Pawluczyk, A. Jozwikowska, J. Rutkowski, and M. Kopytko. Generation-recombination effect in high-temperature HgCdTe heterostructure nonequilibrium photodiodes. *Journal of Electronic Materials*, 38(8), 2008. http://dx.doi.org/10.1007/s11664-009-0752-0.

[43] J. Rothman, N. Baier, P. Ballet, L. Mollard, M. Fournier, J. S. Gout, and J.-P. Chamonal. High-operating-temperature hgcdte avalanche pho-

todiodes. *Journal of Electronic Materials*, 38(8), 2008. http://dx.doi.org/10.1007/s11664-009-0823-2,.

[44] http://en.wikipedia.org/wiki/LIDAR. Visited 01.11.2011.

[45] http://en.wikipedia.org/wiki/Scintillation_counter. Visited 16.09.2011.

[46] A. Bellotti, M. Moresco, and F. Bertazzi. A 2D full-band Monte Carlo study of HgCdTe-based avalanche photodiodes. *Journal of Electronic Materials*, 40(8), 2011. http://dx.doi.org/10.1007/s11664-011-1635-8.

[47] R. Haakenaasen. HgCdTe state-of-the-art photodiode architectures (2010) FFI-rapport 2011/00547. Technical report, Norwegian Defense Research Establishment (FFI), 2011. BEGRENSET.

[48] B. K. Ridley. *Quantum Processes in Semiconductors*. Oxford Science Publications, 1982.

[49] R. F. Pierret. *Semiconductor Device Fundamentals*. Addison-Wesley, 1996. Reproduced at http://www-ee.ccny.cuny.edu/www/web/crouse/EE339/Lectures/RecombGen.htm, visited 11.07.2011.

[50] S. Derelle, S. Bernhardt, R. Haïdar, J. Primot, J. Deschamps, J. Rothman, and G. Perrais. A Monte Carlo study of multiplication and noise in HgCdTe avalanche photodiodes. In *Proceedings of SPIE*, volume 7003, 2008. http://dx.doi.org/10.1117/12.780501.

[51] S. Derelle, S. Bernhardt, R. Haïdar, J. Primot, J. Deschamps, and J. Rothman. A Monte Carlo study of $Hg_{0.7}Cd_{0.3}Te$ e-APD. *IEEE Transactions on Electronic Devices*, 56(04), 2009. http://dx.doi.org/10.1109/TED.2009.2012526.

[52] M. A. Kinch, J. D. Beck, C.-F. Wan, F. Ma, and J. Campbell. HgCdTe electron avalanche photodiodes. *Journal of Electronic Materials*, 33(6), 2004. http://dx.doi.org/10.1007/s11664-004-0058-1.

[53] F. Bertazzi, M. Moresco, M. Penna, M. Goano, and E. Bellotti. Full-band Monte Carlo simulation of HgCdTe APDs. *Journal of Electronic Materials*, 39(7), 2010. http://dx.doi.org/10.1007/s11664-010-1198-0.

[54] M. Moresco, F. Bertazzi, and E. Bellotti. GaN avalanche photodetectors: A full band Monte Carlo study of gain, noise and bandwidth.

IEEE Journal of Quantum Electronics, 47(4), 2011. http://dx.doi.org/10.1109/JQE.2010.2091257.

[55] G. Perrais, S. Derelle, L. Mollard, J. Chamonal, G. Destefanis, G. Vincent, S. Bernhardt, and J. Rothman. Study of the transit-time limitations of the impulse response in mid-wave infrared HgCdTe avalanche photodiodes. *Journal of Electronic Materials*, 38(8), 2009. http://dx.doi.org/10.1007/s11664-009-0802-7.